UPPSALA
UNIVERSITET

Digital Comprehensive Summaries of Uppsala Dissertations from the Faculty of Science and Technology 626

Resonant Soft X-ray Spectroscopic Studies of Light Actinides and Copper Systems

ANDERS MODIN

ACTA
UNIVERSITATIS
UPSALIENSIS
UPPSALA
2009

ISSN 1651-6214
ISBN 978-91-554-7476-8
urn:nbn:se:uu:diva-100221

Dissertation presented at Uppsala University to be publicly examined in Polhemsalen, Ångströmlaboratoriet, Lägerhyddsvägen 1, Uppsala, Friday, May 8, 2009 at 13:15 for the degree of Doctor of Philosophy. The examination will be conducted in English.

Abstract
Modin, A. 2009. Resonant Soft X-ray Spectroscopic Studies of Light Actinides and Copper Systems. Acta Universitatis Upsaliensis. *Digital Comprehensive Summaries of Uppsala Dissertations from the Faculty of Science and Technology* 626. 63 pp. Uppsala. ISBN 978-91-554-7476-8.

Light actinides and copper systems were studied using resonant soft X-ray spectroscopy.

An instrumental and experimental setup for soft X-ray spectroscopy meeting the requirements of a closed source for radioactivity was developed and described in detail. The setup was used for studies of single-crystal PuO_2 oxidation. The existence of higher oxidation state than Pu(IV) in some surface areas of the single crystal were found from O 1s X-ray absorption measurements. Furthermore, from comparison with first principles calculations it was indicated that plutonium oxide with Pu fraction in a higher oxidation state than Pu(IV) consists of inequivalent sites with $Pu^{(IV)}O_2$ and $Pu^{(V)}O_2$ rather than a system where the Pu oxidation state is constantly fluctuating between Pu(IV) an Pu(V).

It was shown that a combination of resonant O Kα X-ray emission and O 1s X-ray absorption spectroscopies can be used to study electron correlation effects in light-actinide dioxides.

The electronic structure of copper systems was studied using resonant inelastic soft X-ray scattering and absorption spectroscopy. It was found that X-ray absorption can be used to monitor changes in the oxidation state but as differences between systems with the same oxidation state are in many cases small, speciation is uncertain. Therefore, a method utilizing resonant inelastic X-ray scattering as fingerprint to characterize complex copper systems was developed. The data recorded at certain excitation energies revealed unambiguous spectral fingerprints for different divalent copper systems. These specific spectral fingerprints were then used to study copper films exposed to different solutions. In particular, it was shown that resonant inelastic X-ray scattering can be used *in situ* to distinguish between CuO and $Cu(OH)_2$, which is difficult with other techniques.

Keywords: Resonat soft X-ray spectroscopy, Resonant inelastic X-ray scattering, X-ray emission, X-ray absorption, actinides, copper systems

Anders Modin, Department of Physics and Materials Science, Atomic and molecular physics, Box 530, Uppsala University, SE-75121 Uppsala, Sweden

ISSN 1651-6214
ISBN 978-91-554-7476-8
urn:nbn:se:uu:diva-100221 (http://urn.kb.se/resolve?urn=urn:nbn:se:uu:diva-100221)

To my parents

List of Papers

This thesis is based on the following papers, which are referred to in the text by their Roman numerals.

I **Closed source experimental system for soft X-ray spectroscopy of radioactive materials,** A. Modin, S. M. Butorin, J. Vegelius, A. Olsson, C.-J. Englund, J. Andersson, L. Werme, J. Nordgren, T. Käämbre, G. Skarnemark, and B. E. Burakov, Rev. Sci. Instrum. 79, 093103 (2008)

II **Indication of single-crystal PuO_2 oxidation from O 1s X-ray absorption spectra,** A. Modin, Y. Yun, M.-T. Suzuki, J. Vegelius, L. Werme, J. Nordgren, P. M. Oppeneer, and S. M. Butorin, in manuscript

III **Correlation effects in dioxides of light actinides studied by O 1s X-ray absorption and X-ray emission spectroscopies,** A. Modin, M.-T. Suzuki, J. Vegelius, Y. Yun, D. K. Shuh, L. Werme, J. Nordgren, P. M. Oppeneer, and S. M. Butorin, in manuscript

IV **Reduction of Pu(VI) on Fe surfaces: soft X-ray absorption and resonant inelastic scattering study,** S. M. Butorin, K. O. Kvashnina, A. Modin, J.-H. Guo, D. K. Shuh, L. Werme, and J. Nordgren,
Final activity report to the European Comission, EC Contract, NF-PRO, FI6W-CT-2003-02389 (2007) also SKB TR-09-08 (2009)

V **Changes in electronic structure of copper films in aqueous solutions,** K. O. Kvashnina, S. M. Butorin, A. Modin, I. Soroka, M. Marcellini, J.-H. Guo, L. Werme, and J. Nordgren, J. Phys.: Condens. Matter 19, 226002 (2007)

VI **In situ X-ray absorption study of copper films in ground water solutions,** K. O. Kvashnina, S. M. Butorin, A. Modin, I. Soroka, M. Marcellini, J. Nordgren, J.-H. Guo, and L. Werme, Chemical Physics Letters, 447 (2007)

VII **Resonant inelastic X-ray scattering as fingerprint for characterization of complex copper systems,** A. Modin, K. O. Kvashnina, S. M. Butorin, L. Werme, and J. Nordgren, in manuscript

VIII **Electronic structure of complex copper compounds probed by resonant inelastic X-ray scattering at Cu L_3 edge,** K. O. Kvashnina, S. M. Butorin, A. Modin, J.-H. Guo, R. Berger, L. Werme and J. Nordgren, in manuscript

IX **Electronic structure of Cu_3N films studied by soft X-ray spectroscopy,** A. Modin, K. O. Kvashnina, S. M. Butorin, L. Werme,

J. Nordgren, S. Arapan, R. Ahuja, A. Fallberg, and M. Ottosson, J. Phys.: Condens. Matter 20, 235212 (2008)

Reprints were made with permission from the publishers.

The following article has been omitted from the thesis due to the character of the material and my limited contribution.

- **X-ray absorption and emission study of hydrogenated fullerenes**, K. O. Kvashnina, J.-H. Guo, A. V. Talyzin, A. Modin, T. Kaambre, S. M. Butorin, and J. Nordgren, AIP Conf. Proc. 837, 230 (2006)

Also my input to the Uppsala book series in atomic and molecular physics have been omitted due to the textbook nature of the material and my limited contribution.

- **Atom och Molekylfysik**, S. Andersson, F. Bruhn, J. Hedman, L. Karlsson, S. Lunell, K. Nilson and J. Wall, Repro Fysikum, Uppsala (2005)

Contents

1. Introduction

Spectroscopic studies of the light emitted or absorbed by atoms date from the early nineteenth century and today, spectroscopy is a powerful method in modern physics. Especially important for studying electronic properties is light in the range of soft X-rays, which interacts with electrons in the studied systems, with strength that varies with the photon energy. The introduction of the third generation synchrotron sources, have made possible spectroscopic studies of highly complex systems due to the extremely high-brilliance light generated in the soft X-ray region.

Actinide materials have attracted growing attention from researchers within the past couple of decades since their electronic structures and macroscopic properties are strongly affected by the dual, localized versus delocalized nature of the 5f electrons. These compounds are also interesting from a technological point of view as they play a major role in the nuclear fuel cycle.

In the Swedish concept for final disposal of nuclear waste, the spent nuclear fuel is encapsulated in copper canisters with cast iron insert. The impermeable copper canisters are then placed in crystalline basement rock at a depth of about 500 meters, embedded in bentonite clay. Since the underground repository is an oxygen free environment, the corrosion of the copper canisters is controlled by the availability of corrosive groundwater components, mainly sulfide, circulating around the canisters.

Safe disposal of nuclear waste requires clear understanding of the behavior of actinides in various forms of the waste, as well as of the interaction of the copper canister with the surrounding environment in the repository.

In this thesis, I present the results of resonant soft X-ray spectroscopic studies of the light actinides; uranium, neptunium and plutonium (papers I - IV) together with the outcome of *in situ* soft X-ray spectroscopic investigations of copper corrosion (papers V - IX).

The thesis is organized in the following way: In Chapter 2, soft X-ray spectroscopy and some physical background to facilitate understanding of the experimental results are introduced. Chapter 3, describes the main characteristics of synchrotron radiation sources as well as some important equipment for collection of experimental data. Finally, the results of my research are summarized in Chapter 4, were the outcomes of the actinide studies are outlined in Chapter 4.1 and the main points of the copper results are given in Chapter 4.2.

2. Atomic structure and soft X-ray spectroscopy

The principal part of my research have been focused on using soft X-ray spectroscopies for studies of the electronic structure in atoms and molecules involved in the nuclear waste cycle.

In this chapter, soft X-ray spectroscopy and some physical background to facilitate understanding of the experiments are introduced.

2.1 Atomic and molecular physics

Today's atomic picture originates from Rutherford's idea of a small heavy nucleus with a "cloud" of light electrons at some distance from the core [1]. Niels Bohr later used Rutherford's results and by postulating that the electrons could only move in specific circular orbits, without emitting radiation as in classical physics, he was able to derive the value of Rydbergs constant and thus could calculate the energy levels of hydrogen [2, 3, 4]. This semiclassical model, where the quantization was postulated and not based on fundamental physics, was not fully satisfactory. The insight of the wave-particle duality for matter and energy on the atomic scale, led to the formulation of Schrödinger's equation [5], which forms the basis for the quantum mechanical description of the atom that we use today.

2.1.1 The Schrödinger equation

Schrödinger's equation uses the wave-particle duality to include all the information of a system in a wave function. The equation can be expressed on the form

$$\left(\frac{-\hbar^2}{2m}\nabla^2 + V(\mathbf{r},t)\right)\Psi(\mathbf{r},t) = i\hbar\frac{\partial}{\partial t}\Psi(\mathbf{r},t) \tag{2.1}$$

where $V(\mathbf{r},t)$ and $\Psi(\mathbf{r},t)$ are the time and space dependent potential and wave function respectively. By assuming that the Schrödinger equation can be written as a separable time-independent part and a time-dependent part,

$\Psi(\mathbf{r},t) = \Psi(\mathbf{r})\Phi(t)$, Eq. 2.1 reduces to a time-independent equation

$$\left(\frac{-\hbar^2}{2m}\nabla^2 + V(\mathbf{r})\right)\Psi(\mathbf{r}) = E\Psi(\mathbf{r}) \tag{2.2}$$

and one time-dependent equation

$$E\phi(t) = i\hbar\frac{\partial}{\partial t}\Phi(t) \tag{2.3}$$

The time-independent Schrödinger equation can be written as

$$\hat{H}\Psi(\mathbf{r}) = E\Psi(\mathbf{r}) \tag{2.4}$$

which is an eigenvalue equation, where $\hat{H}$ is an operator called the Hamiltonian, $\Psi(\mathbf{r})$ is the wave function (eigenfunction) describing the state of the system and E is the energy eigenvalue of the Hamiltonian operator.

The wave function contains all the dynamical information of the system it describes. Max Born interpreted $\Psi(\mathbf{r})$ as a probability amplitude for some point $\mathbf{r}$ in space, and thus, the square of the wave function $|\Psi(\mathbf{r})|^2$is proportional to the probability of finding the particle at that point [6, 7]. This interpretation together with the Schrödinger equation itself implies severe mathematical restrictions to possible $\Psi(\mathbf{r})$. An acceptable wave function must be continuous, have a continuous slope, be single valued and be finite everywhere. In addition $\Psi(\mathbf{r})$ cannot be zero everywhere as the particle it describes must be somewhere, see e.g. Chapter 13.4 in Atkins' book [8]. These severe restrictions implies that the acceptable wave functions are standing waves and thus quantized with quantized energy eigenvalues.

2.1.2 Atomic structure

Schrödinger's equation can be solved analytically exact for hydrogen-like systems while the solution for systems with three particles or more, must be approximative due to coupling of differential equations. Hydrogen-like systems are two-body problems with a heavy nucleus, which can be assumed to be stationary, and an electron moving in a central field Coulomb-potential. Thus, the one electron Hamiltonian in spherical coordinates becomes

$$\hat{H} = \frac{-\hbar^2}{2m}\nabla^2 - \frac{Ze^2}{4\pi\varepsilon_0 r} \tag{2.5}$$

where Z is the number of protons in the nucleus, e is the electronic charge, m is the reduced mass, ε_0 is the permittivity of vacuum and r is the radial position of the electron. Using this Hamiltonian, the solution of Eq. 2.4 is a product of

radial functions $R_{nl}(r)$ and spherical harmonics $Y_{lm_l}(\phi,\theta)$ such that:

$$\Psi_{n,l,m_l}(r,\phi,\theta) = R_{nl}(r)Y_{lm_l}(\phi,\theta) \tag{2.6}$$

where n, l and m_l are quantum numbers introduced in the solution to ensure that the wave function is an acceptable physical solution. The quantum number n is the principal quantum number, which is related to the radial position of the electron. The quantum number l is the angular momentum quantum number and reflects the electron's orbital momentum. The quantum number m_l is the magnetic quantum number representing the angular momentum projection along the z-axis. In addition to these three quantum numbers, the projection along the z-axis for the intrinsic angular momentum of the electron gives the spin projection quantum number m_s.

$$\begin{aligned} n = &\quad 1,2,3\ldots && n \geq 1 \\ l = &\quad 1,2,3,\ldots,n && l \leq n \\ m_l = &\quad 0,\pm1,\pm2,\ldots,\pm l && l \geq m_l \geq -l \\ m_s = &\quad \pm\tfrac{1}{2} && m_s = \pm\tfrac{1}{2} \end{aligned}$$

All electrons with a given value of n form a single *shell* in an atom. Electrons with the same value of n but with different values of l form *orbitals* within the given shell. In spectroscopy shells and orbitals are commonly denoted:

$$\begin{array}{rcccccc} n = & 1 & 2 & 3 & 4 & 5 & 6\ldots \\ & K & L & M & N & O & P\ldots \\ l = & 0 & 1 & 2 & 3 & 4 & 5\ldots \\ & s & p & d & f & g & h\ldots \end{array}$$

To visualize an orbital's distribution in space, the most common is to draw an electron contour surface including 90% of the electron density $|\Psi_{n,l,m_l}(r,\phi,\theta)|^2$. Fig. 2.1 shows such a picture for s, p and d orbitals.

The orbital energies are $(2l+1)$-fold degenerate with respect to the magnetic quantum number m_l. An additional 2-fold energy degeneracy stems from the spin quantum number m_s. For atoms with more than one electron the mutual Coulomb repulsion between electrons causes splitting of the l-orbital energies. If relativistic effects are taken into account, the spin-orbit interaction causes further splitting of the orbital energies, due to electromagnetic interaction between the electron's spin and the nucleus's electric field.

The splitting of orbital energy levels is more pronounced for heavier many-electron atoms such as rare-earths. For such atoms l, m_l and m_s are no longer valid quantum numbers as they do not commute with the Hamiltonian, and thus, other quantum numbers are needed. These includes a total angular momentum quantum number J, the projection of the total angular momentum quantum number along the z-axis M_J and parity.

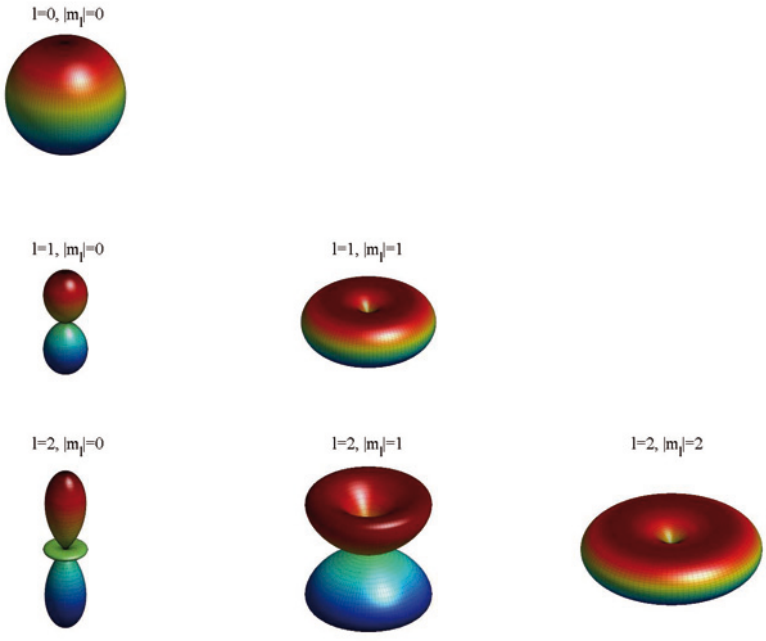

Figure 2.1: Electron contour surface including 90% of the electron density $|\Psi_{n,l,m_l}(r,\phi,\theta)|^2$ for s, p and d orbitals.

2.1.3 The structure of many-electron atoms

For atoms containing N electrons, with $N > 1$, no exact solution to Schrödinger's equation can be obtained due to coupling of differential equations.

The N electrons fill the shells and orbitals of an atom according to the *Aufbau* principle where the number of electrons that can occupy each orbital is limited by the Pauli exclusion principle [9]. The arrangement of electrons according to this principle result in an electron configuration for the atom. The electron configuration is given on the form $(nl)^{x_1}(n_l)^{x2}\cdots(nl)^{x_y}$. For example divalent copper Cu^{2+} has the electron configuration $1s^2 2s^2 2p^6 3s^2 3p^6 3d^9$, or simply $3d^9$.

In spectroscopy, another common way to indicate a certain state for many-electron atoms is through coupling of the one-electron quantum numbers into a so-called term symbol. This coupling of angular momenta can be done in several ways. Usually the chosen coupling scheme for an atom corresponds to the coupling of successive momenta in the order of decreasing strength of the various interactions.

For light atoms, the electrons mutual Coulomb repulsion is the strongest interaction. As this interaction only affect the orbital angular momenta and not the spin, all angular momenta are first coupled together to give a total

angular momentum L of the atom. Similarly all spin momenta are coupled to a total spin momentum S. L and S are then coupled together to give the total angular momentum J of the N-electron atom. This scheme is known as the LS (Russell-Saunders) coupling scheme [10] and is usually summarized in a term symbol $^{2S+1}L_J$. For closed shells there are no resulting angular momentum or resulting spin. Thus, only electrons outside closed shells contribute to L, S and J. The values of L, S and J are obtained by using the Clebsch-Gordan series:

$$\begin{aligned} L = &\quad l_1+l_2, l_1+l_2-1, l_1+l_2-2, \ldots, |l_1-l_2| \\ S = &\quad s_1+s_2, s_1+s_2-1, s_1+s_2-2, \ldots, |s_1-s_2| \\ J = &\quad L+S, L+S-1, L+S-2, \ldots, |L-S| \end{aligned}$$

The naming convention for total orbital angular momentum L follows the convention of orbitals l but with capital letters, i.e. $L = 0, 1, 2, 3\ldots$ are denoted $S, P, D, F\ldots$.

For heavier atoms with high spin orbit interaction, a jj-coupling scheme is used. In jj-coupling each contributing electrons l_i and s_i are coupled to an electronic j_i ($j_i = l_i + s_i$) and then all electronic j_i's are coupled to a total J:

$$\begin{aligned} j_i = &\quad l_i + s_i \\ J = &\quad j_1+j_2, j_1+j_2-1, j_1+j_2-2, \ldots, |j_1-j_2| \end{aligned}$$

In analogy with the one-electron L, S and J's projection along the z-axis are denoted: M_L, M_S and M_J respectively.

In some contexts also the parity is included in the term symbol. The parity can be calculated from

$$\pi = (-1)^{\Sigma_i l_i} \tag{2.7}$$

where, l_i is the orbital angular momentum for electrons contributing to the term symbol. Parity, if included, is usually indicated with a subscript letter "g" or "u", standing for gerade (German for 'even') or ungerade ('odd').

For the example of divalent copper Cu^{2+} ($1s^2 2s^2 2p^6 3s^2 3p^6 3d^9$) only the atoms in the $3d$ orbital contributes to the term. As orbital holes are equivalent with orbital electrons when deriving a term symbol, divalent copper have $^2D_{5/2,g}$ and $^2D_{3/2,g}$ term symbols under LS coupling.

2.2 Electromagnetic radiation

Electromagnetic (EM) radiation takes the form of waves that propagates in time and space. EM radiation is characterized by its wavelength, where visible light ranges from $\sim 400-700$ nm and the more energetic soft X-ray region used in my research are in the range $\sim 1-10$ nm, see Fig. 2.2.

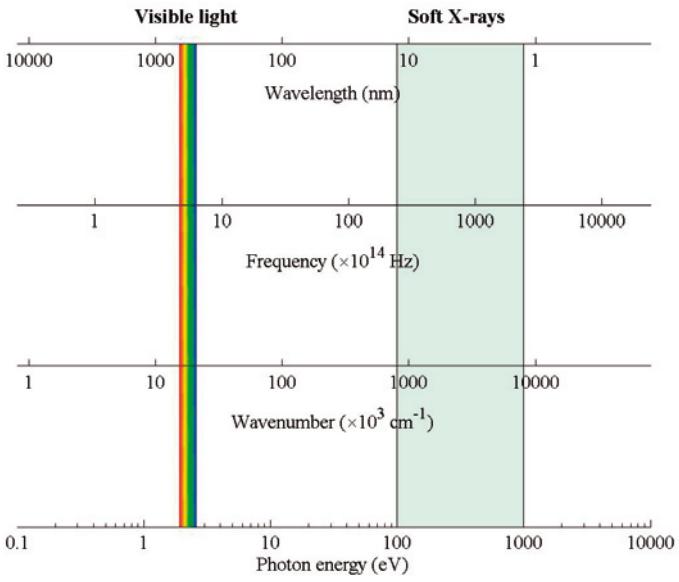

Figure 2.2: Schematic picture of the electromagnetic spectrum on a logarithmic scale.

On the atomic scale, electromagnetic radiation exhibits wave-particle duality and must be treated quantum mechanically. The quantum of EM radiation is called a *photon*. A photon carries energy and momentum that may be imparted when it interacts with matter. The angular momentum is ς ($\varsigma = 1,2,3,\ldots$) in units of $\hbar$ and the energy is given by Planck's law

$$E = h\nu = \frac{hc}{\lambda}, \tag{2.8}$$

where h is Planck's constant, ν is the frequency, c is the speed of light and λ is the wavelength of the electromagnetic radiation.

2.2.1 Interaction of light with matter

The interaction between light and matter is one of the primary experimental areas for probing the properties of solids. The most important interaction in my research is the event where photons interact with the target atom's electrons, transferring energy and is then either absorbed or moves on.

If electromagnetic radiation interacts with electrons, the interaction Hamiltonian can be written as

$$
\begin{aligned}
H_{int} &= \sum_i \Big[-\frac{e}{mc}\mathbf{p}_i \cdot \mathbf{A}(\mathbf{r}_i,t) \\
&\quad + \frac{e^2}{2mc^2}\mathbf{A}(\mathbf{r}_i,t)\cdot\mathbf{A}(\mathbf{r}_i,t) \\
&\quad - \frac{e\hbar}{2mc}\boldsymbol{\sigma}_i \cdot [\nabla \times \mathbf{A}(\mathbf{r},t)]_{\mathbf{r}=\mathbf{r}_i}\Big],
\end{aligned} \tag{2.9}
$$

where the summation is over all participating electrons, $\mathbf{p}_i$ is a differential operator, $\boldsymbol{\sigma}_i$ is the spin and the quantized field operator $\mathbf{A}(\mathbf{r}_i,t)$ is given by

$$
\mathbf{A}(\mathbf{r},t) = \frac{c}{\sqrt{V}}\sum_{\mathbf{k}}\sum_{\alpha}\sqrt{\frac{\hbar}{2\omega}}[a_{\mathbf{k},\alpha}\boldsymbol{\varepsilon}^{(\alpha)}e^{i\mathbf{k}\cdot\mathbf{r}-i\omega t} + a^{\dagger}_{\mathbf{k},\alpha}\boldsymbol{\varepsilon}^{(\alpha)}e^{-i\mathbf{k}\cdot\mathbf{r}+i\omega t}]. \tag{2.10}
$$

Here $a_{\mathbf{k},\alpha}e^{-i\omega t}$ and $a^{\dagger}_{\mathbf{k},\alpha}e^{i\omega t}$ are annihilation and creation operators, decreasing or increasing the number of photons with one. V is a normalization volume and k, $\boldsymbol{\varepsilon}^{(\alpha)}$ and ω are the momentum vector, polarization and angular frequency of the photon respectively.

The first two parts of the interaction Hamiltonian in Eq. 2.10 describes the electrons interaction with the electric field while the last part defines the interaction with the magnetic field. As the main interest here is electronic transitions, the spin magnetic interaction can be ignored. The electric field interaction is made up of one linear ($\mathbf{p}_i \cdot \mathbf{A}(\mathbf{r}_i,t)$) and one quadratic term ($\mathbf{A}(\mathbf{r}_i,t)\cdot\mathbf{A}(\mathbf{r}_i,t)$). From Eq. 2.10 it is evident that a quadratic behavior will change the photon number by two or not at all while the linear term will change the number of photons by ± 1. In the case of absorption/emission, the photon number change only with one and thus, only the $\mathbf{p}_i \cdot \mathbf{A}(\mathbf{r}_i,t)$ terms will contribute to the interaction.

The transition rate per unit time into a solid angle element $d\Omega$ from an initial state Ψ_i to a final state Ψ_f is given by Fermi's golden rule, which in first order perturbation is in the form

$$
W_{d\Omega} = \frac{2\pi}{\hbar}|\langle\Psi_f|H_{int}|\Psi_i\rangle|^2\rho_{\hbar\omega,d\Omega}\times\delta_{(E_f-E_i\pm\hbar\omega)}, \tag{2.11}
$$

where Ψ_i and Ψ_f are the initial and final state with energies E_i and E_f respectively. The delta function ensures energy conservation in the system, i.e. $E_f - E_i \pm \hbar\omega = 0$ and $\rho_{\hbar\omega,d\Omega} = \frac{V\omega^2 d\Omega}{(2\pi)^3\hbar c^3}$ is the density of states in solid angle $d\Omega$.

Transition rates for X-ray emission and absorption can now be obtained by inserting the appropriate interaction Hamiltonian. Assuming energy conservation in the system the transition rate for X-ray absorption yields

$$
\begin{aligned}
W^A_{d\Omega} &= \frac{2\pi}{\hbar}|\langle\Psi_f; n_{\mathbf{k},\alpha}-1|\sum_i -\frac{e}{mc}\mathbf{p}_i\cdot\mathbf{A}(\mathbf{r}_i,t)|\Psi_i; n_{\mathbf{k},\alpha}\rangle|^2\rho_{\hbar\omega,d\Omega} \\
&= \frac{n_{\mathbf{k},\alpha}e^2\omega}{8\pi^2m^2\hbar c^3}\left|\sum_i\langle\Psi_f|e^{i\mathbf{k}\cdot\mathbf{r}_i}\mathbf{p}_i\cdot\boldsymbol{\varepsilon}^{(\alpha)}|\Psi_i\rangle e^{-i\omega t}\right|^2 d\Omega, \qquad (2.12)
\end{aligned}
$$

while the transition rate for X-ray emission is in the form

$$
\begin{aligned}
W^E_{d\Omega} &= \frac{2\pi}{\hbar}|\langle\Psi_f; n_{\mathbf{k},\alpha}+1|\sum_i -\frac{e}{mc}\mathbf{p}_i\cdot\mathbf{A}(\mathbf{r}_i,t)|\Psi_i; n_{\mathbf{k},\alpha}\rangle|^2\rho_{\hbar\omega,d\Omega} \\
&= \frac{(n_{\mathbf{k},\alpha}+1)e^2\omega}{8\pi^2m^2\hbar c^3}\left|\sum_i\langle\Psi_f|e^{-i\mathbf{k}\cdot\mathbf{r}_i}\mathbf{p}_i\cdot\boldsymbol{\varepsilon}^{(\alpha)}|\Psi_i\rangle e^{i\omega t}\right|^2 d\Omega, \qquad (2.13)
\end{aligned}
$$

where $n_{\mathbf{k},\alpha}$ is the number of photons in the initial state.

When applying field theory to the X-ray scattering of photons by atomic electrons, the incoming and outgoing photons are represented by states, $(\mathbf{k}_1,\boldsymbol{\varepsilon}^{(\alpha_1)})$ and $(\mathbf{k}_2,\boldsymbol{\varepsilon}^{(\alpha_2)})$ with energies Ω and ω respectively. In X-ray scattering, the quadratic electron-photon interaction term $\mathbf{A}(\mathbf{r}_i,t)\cdot\mathbf{A}(\mathbf{r}_i,t)$ contributes in first order while the linear term $\mathbf{p}_i\cdot\mathbf{A}(\mathbf{r}_i,t)$ contributes in second order due to consecutive absorption-emission or emission-absorption interactions. The scattering cross section (with respect to the solid angle $\Omega_{\mathbf{k}2}$ and energy ω of the scattered photon) is given by Kramers-Heisenberg [11] scattering formula

$$
\frac{d^2\sigma}{d\Omega_{\mathbf{k}2}d\omega} = \frac{\omega^2}{16\pi^2}\left(\frac{1}{2\pi}\right)^3 W_{12}, \qquad (2.14)
$$

where the transition rate W_{12} is given by

$$
\begin{aligned}
W_{12} &= \sum_f \frac{(2\pi)^3}{\Omega\omega}\left(\frac{e^2}{m}\right)^2\delta_{(E_f-E_g+\omega-\Omega)} \\
&\times\left|\left[\langle\Psi_f|\rho_{\mathbf{k}_1-\mathbf{k}_1}|\Psi_g\rangle(\boldsymbol{\varepsilon}^{(\alpha_1)}\cdot\boldsymbol{\varepsilon}^{(\alpha_2)})\right.\right. \\
&-\frac{1}{m}\sum_i\left(\frac{\langle\Psi_f|\mathbf{p}(\mathbf{k}_2)\cdot\boldsymbol{\varepsilon}^{(\alpha_2)}|\Psi_i\rangle\langle\Psi_i|\mathbf{p}(-\mathbf{k}_1)\cdot\boldsymbol{\varepsilon}^{(\alpha_1)}|\Psi_g\rangle}{E_i-E_g-\Omega}\right. \\
&\left.\left.+\frac{\langle\Psi_f|\mathbf{p}(\mathbf{k}_1)\cdot\boldsymbol{\varepsilon}^{(\alpha_1)}|\Psi_i\rangle\langle\Psi_i|\mathbf{p}(-\mathbf{k}_2)\cdot\boldsymbol{\varepsilon}^{(\alpha_2)}|\Psi_g\rangle}{E_i-E_g+\omega}\right)\right]\right|^2. \qquad (2.15)
\end{aligned}
$$

Here, $|\Psi_g\rangle$, $|\Psi_i\rangle$ and $|\Psi_f\rangle$ are initial, intermediate and final states of the material system, with energies E_g, E_i and E_f, respectively. The factors $\mathbf{p}(\mathbf{k})$ and $\rho_{\mathbf{k}}$ are defined by $\mathbf{p}(\mathbf{k})=\sum_n\mathbf{p}_n e^{-i\mathbf{k}\cdot\mathbf{r}_n}$ and $\rho_{\mathbf{k}}=\sum_n e^{-i\mathbf{k}\cdot\mathbf{r}_n}$

When the energy of the incident photon Ω is close to core electron excitation threshold $E_i - E_g$, as in the case of resonant inelastic X-ray scattering (RIXS), the second term in the square brackets becomes dominant. At the threshold, the denominator $E_i - E_g - \Omega$ vanishes and the formula breaks down. If the finite lifetime of the intermediate state, due to the life time of a core hole, is taken into account then the energy E_i is replaced by a complex number $E_i + i\Gamma_i$ and the divergence is removed. By removing less contributing terms from Eq. 2.15 and noting that RIXS is usually not measured in absolute intensities, the essential part of the RIXS spectrum can be described as [12]

$$F(\Omega,\omega) = \sum_f \left| \sum_i \frac{\langle \Psi_f | \mathbf{p}(\mathbf{k}_2)\cdot\boldsymbol{\varepsilon}^{(\alpha_2)} | \Psi_i \rangle \langle \Psi_i | \mathbf{p}(-\mathbf{k}_1)\cdot\boldsymbol{\varepsilon}^{(\alpha_1)} | \Psi_g \rangle}{E_g + \Omega - E_i - i\Gamma_i} \right|^2 \times \delta_{(E_g+\Omega-E_f-\omega)}, \tag{2.16}$$

where Γ_i represents spectral broadening due to the corehole lifetime in the intermediate state.

As can be seen from the expression of $F(\Omega,\omega)$, RIXS is the coherent second-order process consisting of the X-ray absorption from $|\Psi_g\rangle$ to $|\Psi_i\rangle$ and the X-ray emission from $|\Psi_i\rangle$ to $|\Psi_f\rangle$. If the final state $|\Psi_f\rangle$ is the same as the initial state $|\Psi_g\rangle$, then the spectrum of Eq. 2.16 describes resonant elastic X-ray scattering, while if $|\Psi_f\rangle$ is not the same as $|\Psi_g\rangle$, it gives the RIXS spectrum. When both cases are combined, $F(\Omega,\omega)$ of Eq. 2.16 is called the resonant X-ray emission spectrum.

2.2.2 Selection rules

The interaction between photons and the target atom's electrons alters the wave function of the system. The possible transitions of a system from one state Ψ_i to another Ψ_f are constrained by *selection rules*.

In general, electromagnetic radiation can be classified into multipoles Eχ (electric) or Mχ (magnetic) of order 2^χ, e.g. E1 for electric dipole, E2 for quadrupole, or E3 for octupole.

The angular momentum of a photon is ς ($\varsigma = 1,2,3,\ldots$) in units of $\hbar$, and its projection along the z-axis is given by $\varsigma_z = \vartheta\hbar$. Since the total angular momentum has to be conserved during a transition, this leads in the case of emission to

$$\mathbf{J_i} = \mathbf{J_f} + \boldsymbol{\varsigma}. \tag{2.17}$$

The corresponding photon quantum numbers ς and ϑ must satisfy

$$|J_i - J_f| \leq \varsigma \leq J_i + J_f \qquad \text{and} \qquad \vartheta = M_{Ji} - M_{Jf}, \tag{2.18}$$

with respect to the atoms quantum numbers J and M_J. In addition parity must also be preserved during a transition, leading to

$$\pi(E\varsigma) = \pi_f \pi_i = (-1)^{\varsigma} \tag{2.19}$$

for electric multipole transitions, and

$$\pi(M\varsigma) = \pi_f \pi_i = (-1)^{\varsigma+1} \tag{2.20}$$

for magnetic multipoles.

Equations 2.18 to 2.20 generate different sets of transition rules depending on the multipole order and type. These sets of transition rules are summarized in Tab. 2.1.

Table 2.1: *Summary of transition rules for electric and magnetic dipole, and quadrupole transitions between the atomic states Ψ_i and Ψ_f.*

Electric dipole	Magnetic dipole	Electric quadrupole	Magnetic quadrupole
ΔJ=0,±1 (not 0→0)		ΔJ=0,±1,±2 (not 0→0) (not 0→1) (not $\frac{1}{2} \rightarrow \frac{1}{2}$)	
$\pi_f = -\pi_i$	$\pi_f = \pi_i$		$\pi_f = -\pi_i$

From Eqs. 2.12, 2.13 and 2.16 it can be seen that the operators between the atomic states Ψ_i and Ψ_f are on the form $e^{\pm i\mathbf{k}\cdot\mathbf{r}}$. By Taylor expansion this can be written as $e^{\pm i\mathbf{k}\cdot\mathbf{r}} = 1 \mp i\mathbf{k}\cdot\mathbf{r} - \frac{\mathbf{k}\cdot\mathbf{r}^2}{2} \ldots$, where the first term is the dipole, the second is the quadrupole and the third is the octupole. When $\mathbf{r}$ is in the range of the Bohr radius ($a_0 \sim$0.529 Å), the size of $\mathbf{k}\cdot\mathbf{r}$ for soft X-rays ($\lambda \sim$ 10-100 Å) is in the range $\frac{2\pi a_0}{\lambda} \sim 0.3 - 0.03$. As these values are squared when calculating transition rates, the dipole transitions dominates. This is often referred to as the *dipole approximation*.

2.3 Soft X-ray spectroscopy

Spectroscopy can be defined as the interaction between energetic particles and matter. The energetic particles used in my research were solely soft X-ray photons. Thus, spectroscopy in this context deals with the interaction between light and matter.

In general, soft X-ray photons are sent into the studied sample, which interacts with the radiation field and absorbs energy by promoting electrons to unoccupied orbitals. The system ends up in an excited intermediate state. This

state is however not stable and will relax to a final state, releasing some of the absorbed energy. A basic excitation (a) and relaxation (b) process is shown in Fig. 2.3 together with an artificial spectrum of the process.

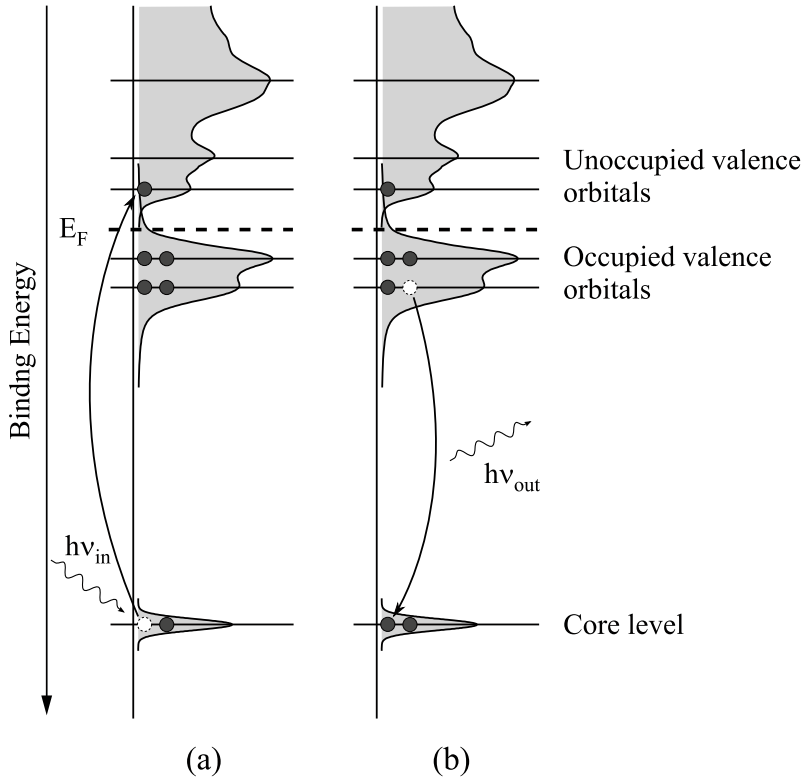

Figure 2.3: A soft X-ray absorption (a) and emission processes (b) in a simplified atom together with fictive spectra of the processes.

The excitation of a sample from the ground state to an intermediate state can be probed using X-ray absorption spectroscopy (XAS), while the relaxation from the intermediate state to the final state can be examined using X-ray emission spectroscopy (XES). In the case when the intermediate state lifetime is too short for the state to delocalize prior to the decay to the final state, resonant inelastic X-ray scattering (RIXS) can be used as probe.

2.3.1 X-ray absorption spectroscopy

In X-ray absorption spectroscopy (XAS), the absorption cross-sections are measured as a function of the incoming photon energy, cf. Eq. 2.12. If the incoming photon energy equals the energy difference between an occupied state and an unoccupied state, a resonance in the absorption spectrum will be

observed. If the photon carries enough energy, the absorption may lead to ionization of the atom. Thus, an X-ray absorption (XA) spectrum is recorded by scanning the excitation energy over the studied absorption edge, see Fig. 2.3 (a).

The core binding energies of most common elements are well separated and the photons can therefore be tuned to a specific atomic site in the studied system. The different absorption edges are in spectroscopy commonly named in accordance with the core level from where the electrons were excited, i.e. $K, L, M, \ldots$ for $n = 1, 2, 3, \ldots$ shells respectively. The position of the edge corresponds to transitions to the lowest allowed unoccupied state and can therefore be used to study the oxidation state of an atom. All transitions are subject to the selection rules depicted in Sec. 2.2.2.

The promotion of a core level electron to an unoccupied state leaves the system in an excited intermediate state. This state is not stable due to the finite life time of a core hole, and will relax by either; emitting a photon with energy less than or equal to the incident photon (radiative decay), or the energy is reabsorbed by a less tightly bound electron, which is emitted (Auger decay). These decay channels can be detected and provides information of the unoccupied states of the studied atom. The radiative channel is commonly denoted fluorescence yield (FY), while Auger decay is called electron yield (EY).

2.3.2 X-ray emission spectroscopy

Whereas XAS probes the unoccupied valence orbitals, X-ray emission spectroscopy (XES) provides information about the occupied states. Thus, the techniques are complementary.

In XES the emitted radiation from a decay of the excited intermediate state is analyzed in its spectral components. The spectral decomposition of the emitted radiation is done with a spectrometer. In my research, the soft X-ray spectrometer described in Sec. 3.2.1 was used for the energy analysis.

Fig. 2.3 (b) visualizes the X-ray emission (XE) process in a simplified atom. The radiative transitions for the excitation and the relaxation of the system are subject to the selection rules described in Sec. 2.2.2. If the excited electron fills the core hole created by the monochromatic photon excitation, the resulting feature in XE spectra is referred to as the elastic peak since the photon is reflected with no energy loss. In all other cases lower energy electrons will fill the core hole giving rise to spectral features at specific energies corresponding to the difference between the energy of the core level and the occupied orbitals. These features are referred to as characteristic or normal emission peaks.

2.3.3 Resonant inelastic X-ray scattering

When the intermediate state lifetime is too short for the state to delocalize prior to the decay to the final state, excitation and decay cannot be considered as separate steps but is rather a one-step process where excitation and decay cannot be separated. This process is referred to as resonant inelastic X-ray scattering (RIXS).

In RIXS, the emitted radiation is analyzed as in the XES case, using the same spectrometer for the spectral decomposition. RIXS spectra are usually collected for several different excitation energies over the studied edge and the spectra are described by Eq. 2.16. Fig. 2.4 shows RIXS-spectra collected over the Ru L_3-edge for RuO_2. It should be noted that the energy scale is not fully calibrated but as the purpose of the figure is to visualize the RIXS process, this is not needed.

The photon excitation used for each spectrum is indicated on the y-axis, while the x-axis gives the emission energy scale. The diagonal features are the elastic peak, corresponding to elastically scattered radiation originating from the RIXS process in which the final state returns to the ground state, followed by resonant inelastic scattering structures at constant energy loss due to an excited final state. The vertical features are characteristic emission lines.

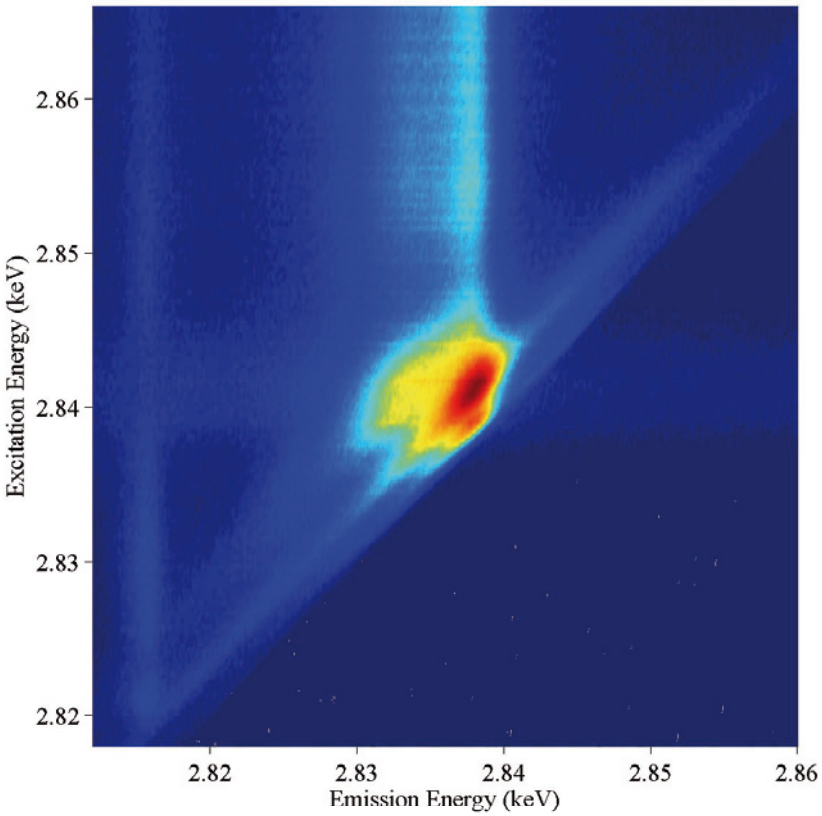

Figure 2.4: Resonant inelastic X-ray spectra for RuO_2 recorded over Ru L_3-edge. The excitation energy used for each spectrum is shown on the y-axis, while the emission energy is shown on the x-axis. The diagonal features are the elastic peak followed by the resonant inelastic scattering structures at constant energy loss. The vertical features are the characteristic emission lines.

3. Experimental environment

As described in the last chapter, spectroscopy deals with the interaction between light and matter. The studied system is disturbed by adding energy in the form of photons and the reaction to this energy input is monitored. As the atomic binding energies lie far above the energies of ordinary light, except for the outermost valence orbitals, all my research have been conducted using more energetic light, i.e. X-rays, from synchrotron radiation sources. Experiments at synchrotrons requires a lot of equipment to make collection of useful data possible.

In this chapter the main characteristics of synchrotron radiation sources, as well as some important equipment for collection of experimental data will be introduced.

3.1 Synchrotron radiation

Synchrotron radiation sources are facilities that produce extremely intense X-rays by accelerating charged particles (usually electrons) orbiting the storage ring at a speed close to the speed of light. Extremely high brightness, high spectral and spatial resolution, polarization possibilities and high flux are among the important features, which makes synchrotrons a powerful tool for scientists.

3.1.1 Storage ring

In the storage ring, electrons are kept circulating at velocities close to the speed of light, under ultra high vacuum to minimize collisions between the fast electrons and other particles. The electrons are kept orbiting the storage ring by means of bending magnets. Whenever the electron orbit is bent in the magnetic fields the electrons are subjected to a central acceleration and radiate in the forward direction. In bending magnets the radiation cone sweeps by a small opening in the magnet. The time it takes for the radiation cone to sweep over this opening is very short due to the very high velocity of the electrons. This gives a wide energy spectrum, with relatively low flux, according to Heisenberg's uncertainty principle.

To increase the flux of the created radiation, magnetic structures can be inserted (called insertion devices) between the bending magnets. There are

two insertion devices in general use, the undulator and the wiggler. As all research presented in this thesis has been done using undulators, only this insertion device will be introduced here. For a more detailed description of undulators, wigglers and bending magnets see Ref. [13].

3.1.2 Undulator radiation

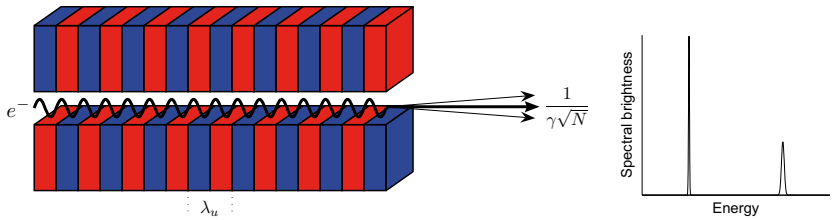

Figure 3.1: Schematic drawing of the magnetic structure, with magnetic period λ_u, of an undulator. The narrow emission cone is shown by arrows and the inserted graph indicates the small energy spread and the high spectral brightness associated with an undulator.

An electron traversing a periodic magnet structure of moderate field strength will undergo a small amplitude oscillation and therefore radiate, see Fig. 3.1. The generated X-rays will have short wavelengths governed by the undulator equation

$$\lambda_n = \frac{\lambda_u}{2\gamma^2 n}(1 + \frac{K^2}{2} + \gamma^2\theta^2) \tag{3.1}$$

where K is the magnetic deflection parameter (K < 1 in the undulator limit), θ is the off-axis angle, γ is the Lorentz factor ($\gamma \equiv 1/\sqrt{1 - v^2/c^2}$) and n is the harmonic number. The radiation of the n:th undulator harmonic is primarily contained in a narrow central radiation cone of half angle

$$\theta_{cen} \simeq \frac{1}{\gamma^*\sqrt{nN}} \tag{3.2}$$

where γ^* is the corrected electron energy defined by $\gamma^* = \gamma/\sqrt{1 + K^2/2}$. This is much smaller than the natural width of the radiation cone ($1/\gamma$). The spectral narrowness of the emission cone leads to extremely high spectral brightness and high flux.

Harmonics are a natural consequence of the motion in an undulator. When high energy photons are hard to generate, higher harmonics are used to increase the energy range of the undulator. There is no radiation produced in-

between the harmonics, see Fig. 3.1, making it necessary to tune the undulator, i.e. move the harmonic peak to the desired energy.

3.1.3 Beamlines

The radiation generated in the undulator is transferred to the experimental station by means of a beamline. In a beamline, the X-rays are monochromatized by a diffracting grating monochromator and focused onto the sample in the experimental station using optics.

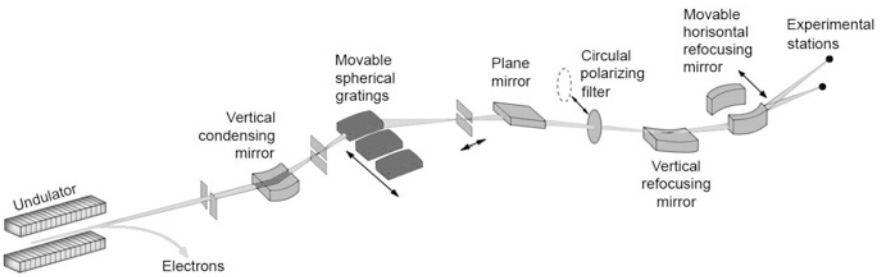

Figure 3.2: Schematic layout of the undulator beamline 7.0.1 at the Advanced Ligth Source, Berkeley, CA, USA.

The experimental work presented in this thesis has been performed on beamline 7.0.1 at the Advanced Light Source (ALS), Berkeley, CA, USA [14] and on beamline I511 at MAX-lab, Lund, Sweden [15].

Beamline 7.0.1 at ALS uses an undulator source with 89 magnetic periods of 5 cm length. Fig. 3.2 schematically shows the experimental arrangement of beamline 7.0.1. The beamline employs a spherical grating monochromator (SGM) with fixed entrance slit and sliding exit slit. A bendable mirror images the exit slit to the experiment, giving a small spot size across the operational range. The undulator gap can be changed as the grating rotates so that the beamline performs at the peaks of the undulator spectrum. The magnetic deflection parameter values can be tuned from K=0.5 to K=2.2, giving a photon energy range from 60 to 1200 eV usable for experiments.

The source for beamline I511 is a hybrid undulator with 99 periods and a period length of 52 mm. The beamline utilizes a modified SX-700 plane grating monochromator (PGM) with a spherical focusing mirror. The refocusing mirrors are a pair of bent elliptical mirrors mounted in a Kirkpatrick-Baez configuration to optimize spot size. The usable energy range for experiments extends from 90 eV to about 1200 eV.

3.2 Experimental equipment

Experiments at synchrotrons requires, as mentioned earlier, a lot of equipment to make collection of useful data possible. This is especially true for soft X-ray experiments as these are conducted under vacuum conditions, and thus need vacuum equipment such as pumps, valves and gauges, in addition to data collection equipment.

There are several standard detectors developed to detect emitted photons from synchrotron radiation experiments, e.g. Multi/Micro Channel Plates (MCP's), channeltrons and photodiodes. In addition to this standard data collection equipment, my experimental research has been carried out using some in-house developed equipment described below.

3.2.1 Grazing incidence spectrometer

All X-ray emission spectroscopic and resonant inelastic X-ray scattering measurements presented in this thesis were performed using a grazing incidence grating spectrometer developed by our group [16, 17] (commercially available from Gammadata AB as Scienta XES350).

The geometry of the spectrometer is based on the Rowland criterion stating that; if a point source is placed on a circle with a radius R tangential with a grating with a radius 2R, it will have its diffracted lines focused on the same circle. A schematic drawing of the working principle of a Rowland spectrometer is shown in Fig. 3.3.

In the spectrometer the different energies of the emitted radiation are separated in space with a diffraction grating according to the grating equation

$$d(sin\theta_m - sin\theta_i) = m\lambda \tag{3.3}$$

where d is the slit spacing, θ_i is the angle between the incident radiation and the grating normal, m is the diffraction order, θ_m is the angle between the outgoing radiation of order m and the grating normal, and λ is the wavelength of the radiation.

Due to the low reflectivity of soft X-rays, the incident angle of the radiation needs to be nearly parallel to the grating surface, i.e. θ_i needs to be close to 90 degrees. Radiation fulfilling this angle criteria is said to be at grazing (or glancing) incidence.

The spectrometer holds three fixed mounted gratings of different radii of curvature and different slit spacings,d. Two of the gold coated, ion etched gratings have a 5 m radius while the third have a 3 m radius. The grove densities are 1200, 400 and 300 slits per mm (i.e. d= .83 , 2.5 and 3.33 μm), providing practical energy ranges of 250-1000 eV, 100-450 eV and 50-250 eV in first order of diffraction respectively.

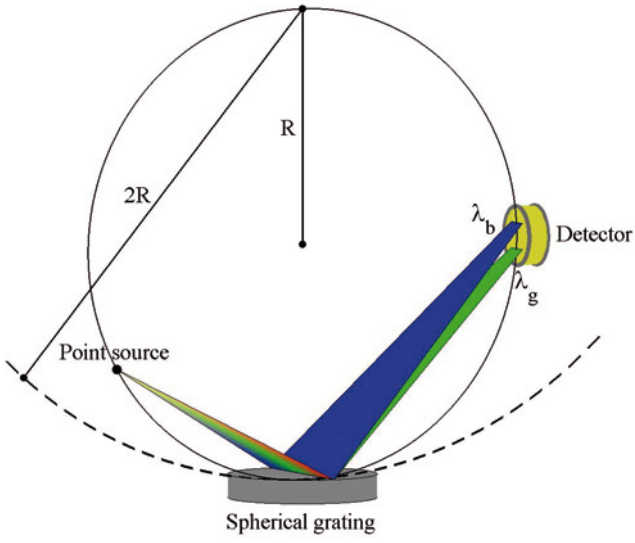

Figure 3.3: Working principle of a grazing incidence Rowland spectrometer. Angles and dimensions of included parts are exaggerated for figure clarity.

The emission lines are recorded by carefully placing a spatially resolving detector tangential to the Rowland circle defined by the grating. The detector is based on two stacks of 50 mm diameter MCP's, arranged with two MCP's in the first stack and three in the second, together with a resistive anode position sensitive detector.

3.2.2 Liquid cells

For the *in situ* measurements of the interaction between copper and liquids in paper V and VI, a small vacuum tight container, refereed to as liquid cell, was used. A photo of a disassembled liquid cell with all parts is shown in Fig. 3.4. The cell is 20 mm in diameter with a thickness of 4 mm. The main part of the liquid cell is machined out of polyetheretherketone (PEEK), an ultra high vacuum (UHV) compatible and chemically inert polymer material. PEEK is also easily machined and electrically insulating. Other materials such as stainless steel, aluminium or copper can also be used to prevent interference with the measurements if the studied sample has X-ray absorption or X-ray emission features in the same energy region as the PEEK cell.

The volume of the cell is kept small, approximately 4 μL, to minimize the effects of window breakage. Further precautions were also taken, such as pin-

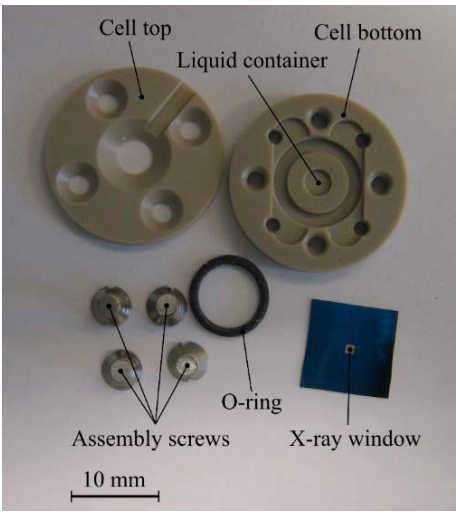

Figure 3.4: Photograph of a disassembled liquid cell with parts labeled.

holes between the experimental chamber and the beamline, and fast interlock systems for protection of the high-voltage detectors.

The soft X-ray window consists of a small thin membrane attached to a 10 mm $\times$ 10 mm silica wafer. The membrane, typically $\sim$0.25-1 mm^2 in area and 100 nm thick, is made of silicon nitride (Si_3N_4) or diamond-like carbon. Silicon nitride membrane windows are commercially available from Silson Ltd, while the carbon windows are made in-house by depositing diamond like carbon on a silicon wafer which is subsequently etched from the back side to expose the carbon film. The membrane allows both the incident and scattered soft X-rays to pass through, making it possible to irradiate the sample and record X-ray emission and absorption spectra. Therefore, the choice of membrane material mostly depends on the desired absorption edges to be studied. Good membrane transmission is necessary in order to acquire well-resolved spectra since strong absorption in the membrane material itself would reduce the signal-to-noise ratio. X-ray transmission for different membranes are readily calculated using the online tool available from Center for X-ray Optics at Lawrence Berkeley Lab [18, 19].

For the *in situ* studies of the chemical reactions between copper and different solutions, a 10 nm copper film was deposited on the backside of a 100 nm silicon nitride window using DC-magnetron sputtering in an ultra high vacuum chamber.

3.2.3 Closed source of radioactivity system

To comply with The Swedish Radiation Protection Authority's (SSI) rules and regulation regarding experiments at MAX-lab on plutonium isotopes [20], an

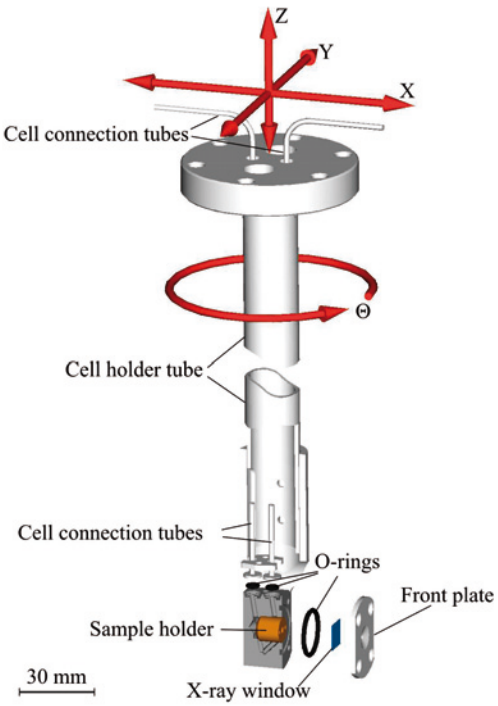

Figure 3.5: Schematic drawing of the closed radioactivity source setup, with parts labeled. The tube connecting the cell with the top CF 40 flange has been shortened for better overview. The standard valves on top of the thin cell connection tubes together with all tubing feedthroughs and screws are left out for clarity.

instrumental and experimental setup for soft X-ray spectroscopy meeting the requirements of a closed source for radioactivity was used for the measurements in paper I. The closed source of radioactivity system is described in detail in paper I and only the main characteristics are introduced here.

Fig. 3.5 shows a schematic picture of the closed source of radioactivity system. The holder for the cell is constructed as a straight tube, with a widening at the top for stability, fitting through a 35 mm inner diameter standard manipulator and attached to the top flange. This enables the use of essentially any standard xyz+θ manipulator setup for mounting. The holder is designed so that the X-ray window is situated on the rotational axis of the manipulator.

The cell connection steel tubes visible at the top of the flange is connected to the inside of the cell. The tubes are connected to the cell by a clamped seal with compressed rubber or viton O-rings. This tubing can be used to pump down the closed source cell in a secure area before sealing the tubes to comply with closed source requirements for transportation and measurements. The sealing of the cell is handled by means of standard manual valves fitted to the top of the cell connection tubes with Swagelok® feedthroughs.

The main part of the cell is machined out of a single piece of PEEK polymer on account of the materials favorable properties discussed in the previous section. The sample holder is a metallic screw to which the sample is attached by glue or any other type of adhesive material. The metal screw can be adjusted to accommodate samples of different height, which is important as the geometry constraints of the setup requires the sample to be placed as close as possible to the X-ray window to assure that the X-rays can hit the sample and the emitted radiation from the sample can reach the detector through the small X-ray window. Placing the sample close to the window also minimizes the absorption of X-rays in the small gap between the window and the sample, resulting in better signal-to-noise ratio.

The front plate is detachable in order to mount samples and X-ray windows. The plate is made of stainless steel or aluminum since these are easily machined and can, therefore, be made sufficiently thin to avoid obstruction of the X-ray path. The front plate is mounted to the main part of the cell with four screws. A large O-ring serves as vacuum seal between the plate and the cell.

The thin X-ray window is mounted on the front plate by means of epoxy glue and separates the vacuum of the analysis chamber from the closed cell. The glue is used both for attaching the window to the front plate and as a vacuum sealant. The soft X-ray windows are of the same type as used in the liquid cells, see Sec. 3.2.2, with the same requirements for choice of membrane material depending on desired absorption edges to be studied. As the purpose of the study using the closed source of radioactivity system was to investigate the electronic structure of PuO_2, a diamond-like carbon membrane window was used to provide the possibility of studying both the Pu 5*d* edge and the O 1*s* absorption edge at energies $\sim$110 eV and $\sim$ 540 eV, respectively.

4. Results

In this section, the results of my research are summarized. The outcomes of the soft X-ray spectroscopic studies of actinides (papers I - IV) are outlined in section 4.1 and the main points of the *in situ* copper investigations (papers V - IX) are given in Chapter 4.2.

4.1 Actinides

Actinide materials have attracted growing attention from researchers within the past couple of decades since their electronic structures and macroscopic properties are strongly affected by the dual, localized versus delocalized nature of the $5f$ electrons. These compounds are also interesting from a technological point of view as they play a major role in the nuclear fuel cycle.

Safe disposal of nuclear waste requires clear understanding of the behavior of actinides in various forms of the waste, as well as of the interaction of these waste forms with the environment.

Theoretical studies of these strongly correlated materials are difficult due to the nonperturbative nature of the problem, and the presence of several competing physical mechanisms, such as localization versus delocalization [21]. In particular, traditional density functional theory (DFT) does not capture the localization effect of the $5f$ electrons originating from the strong intra-atomic electron-electron interaction [22].

Experimental studies of actinides are severely limited due to the toxic and radioactive nature of actinide materials such as PuO_2. Therefore, the closed source of radioactivity system introduced in section 3.2.3 and fully described in paper I was developed to lighten the rules and regulations concerning handling, transportation, and storage of radioactive materials. By that, the possibilities of studying these materials are enhanced.

Most experimental studies of actinide materials have been conducted on the actinide side and very little data are reported for the ligands. To fully understand the correlation effects in actinide materials, also the ligands need to be studied. Therefore, we report soft X-ray spectroscopic studies on both the actinide site, paper IV, and the ligand site in papers I - III.

4.1.1 Oxidation of plutonium dioxide

Plutonium dioxide (PuO_2) has traditionally been considered as the highest stable Pu oxide, but recent findings indicates that PuO_2 can react with water to form higher oxides up to $PuO_{2.27}$ [23]. The existence of PuO_{2+x} will have great consequences for the proposed underground disposal of nuclear waste since higher-oxidation-state plutonium species are much more water soluble than Pu(IV) species and, consequently, more mobile and can be transported from the waste repository to the biosphere[24].

Fig. 4.1 displays X-ray absorption and resonant X-ray scattering spectra of polycrystalline PuO_2 recorded throughout the Pu 5d edge. RIXS spectra which were measured at an energy of the incident photon beam tuned to various parts of the Pu 5d absorption edge are plotted in Fig. 4.1 on the energy loss scale. RIXS spectra reveal a number of structures showing dependence on varying energies of incident photons. In particular, structures at energy losses of -0.8, -1.1, -1.6 and -1.8 eV can be identified in some RIXS spectra. Important resonant behavior can be noted for the -1.6 eV and -1.8 eV structures which are marked by dashed vertical lines in Fig. 4.1. The former is significant in the RIXS spectrum recorded at the excitation energy of 109.5 eV and again becomes pronounced for energies of incident photons being in the range 113-115 eV, while the latter resonates at excitation energies tuned between 110 and 112.5 eV.

According to calculations reported in paper IV, the main RIXS peaks of Pu(V) are shifted to higher energy losses by 0.2 eV which matches exactly the energy difference between structures at -1.6 eV, which is believed to belong to Pu(IV), and at -1.8 eV in the measured RIXS spectra. Due to selectivity properties of the RIXS technique, differences in the absorption and resonant scattering cross-sections for Pu(IV) and Pu(V), it is quite reasonable to expect that the relative intensity of the Pu(V) contribution can be enhanced versus that of Pu(IV) in the RIXS spectra for specific excitation energies. The presence of the Pu(V) fraction in the polycrystalline PuO_2 sample may be due to its preparation procedure or/and specific conditions under which further oxidation of PuO_2 may take place as it has been discussed in scientific literature [23].

The presence of some fraction of Pu in higher oxidation state than Pu(IV) in the polycrystalline PuO_2 sample is also supported by Pu 4*d* X-ray absorption measurements (see Fig. 4.2). The Pu 4*d* X-ray absorption spectrum of the polycrystalline reference sample is shifted to higher-energies by approximately 0.3 eV and narrower as compared to that of the high-activity Pu-on-Fe sample. This behavior indicates higher average charge of Pu atoms in the reference sample. On the other hand, analysis of RIXS spectra does not support the presence of Pu(III) in the Pu-on-Fe samples.

The O 1*s* X-ray absorption spectra of single crystal plutonium dioxide were measured for a number of randomly selected areas on the surface of the single crystal. Figure 4.3 shows XA spectra collected from three different areas on the surface of the single crystal (SC) together with XA spectrum for polycrys-

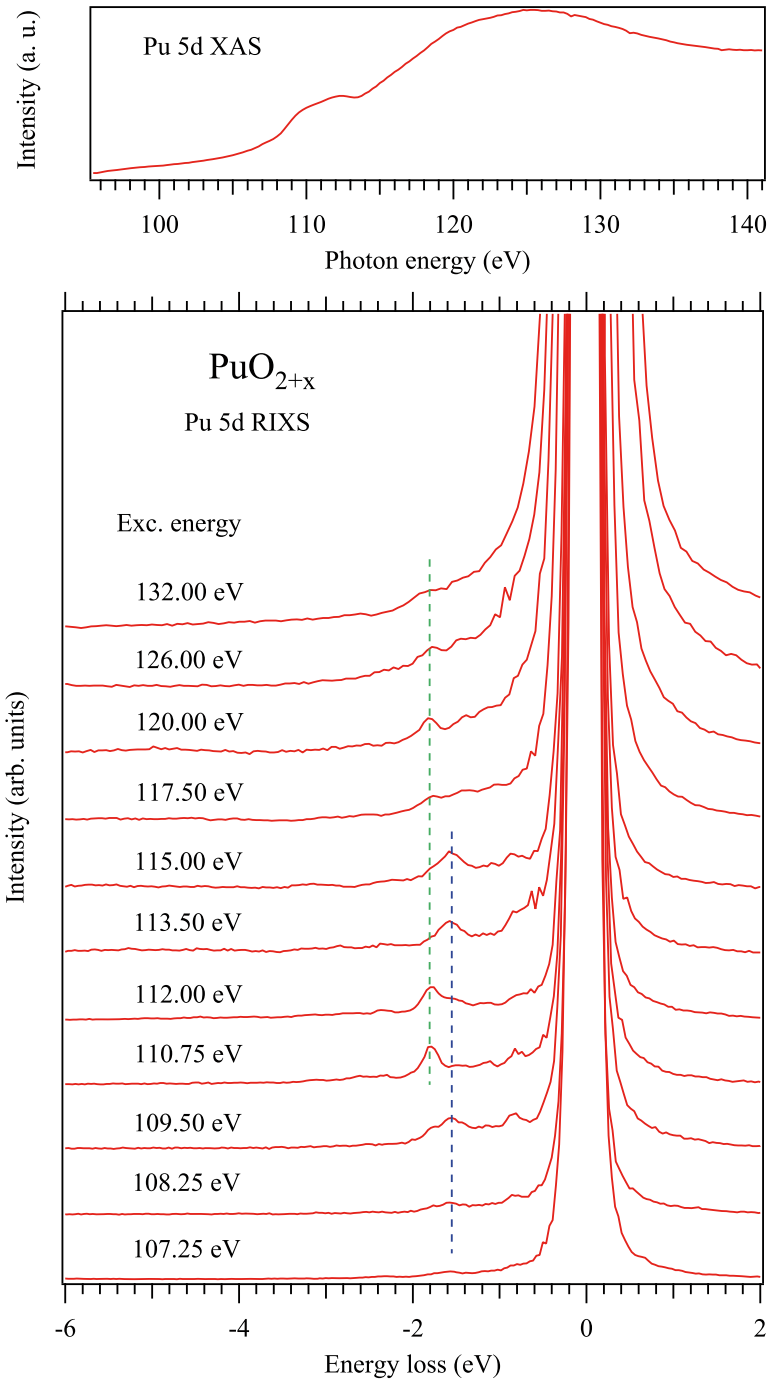

Figure 4.1: Resonant X-ray scattering spectra of the polycrystalline Pu dioxide sample recorded at different excitation energies close to the Pu 5d threshold. The Pu 5d absorption edge recorded in the total electron yield mode is shown in the top panel.

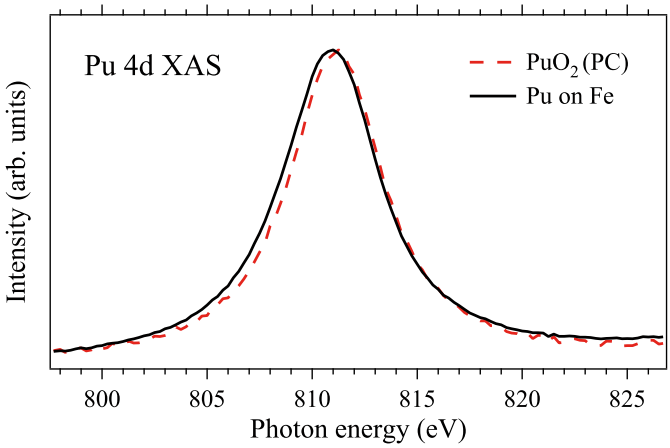

Figure 4.2: Total electron yield spectra of the polycrystalline Pu dioxide reference and Pu sorbed on Fe foil across the U 4d absorption edge.

talline (PC) PuO_2. All spectra have similar main spectral features with structures around 531, 533.4, 538.3, 539, 541.7 and 544.5 eV. There is, however, a significant difference in intensity for the first two peaks between different areas on the surface of the single crystal and the polycrystalline sample. It is clear that the structure at $\sim$ 531 eV has the lowest intensity for the polycrystalline sample, while all spots measured on the single crystal show higher intensity for this feature. Nevertheless, for some spots the spectral intensity at $\sim$ 531 eV approaches that of the polycrystalline sample. The theoretical results presented in paper II show that this peak can be attributed to O 2p-Pu 5f hybridization while the peak at $\sim$ 533.4 eV arises from hybridization with Pu d-states.

To understand the observed spectral changes, a number of different defect structures $PuO_{2\pm x}$ were calculated using the generalized gradient approximation, with intra-atomic Coulomb interaction-U added for f-electrons (GGA+U). All the studied defect structures; Pu_8O_{15}, Pu_7O_{16} , Pu_4O_9, Pu_8O_{17}, and the Pu_8O_{17} cluster calculation, were calculated using U= 5 eV. The resulting density of states (DOS) was appropriately broadened to simulate XA spectra. The broadening was consequently performed with Lorentzian and Gaussian function to account for the O 1s core hole lifetime, instrument resolution and other broadening effects, respectively.

The broadened partial O 2p DOS spectra for all defect calculations together with that of stoichiometric PuO_2 and experimentally recorded XA spectrum for the single crystal sample are shown in in Fig.4.4.

All calculated absorption spectra show increased intensity in the O 2p-Pu 5f hybridization feature for the defect structures $PuO_{2\pm x}$ compared to stoichiometric PuO_2, while all but Pu_8O_{15} exhibit decreased intensity in the second peak. In particular, the absorption spectra for Pu_8O_{17} and

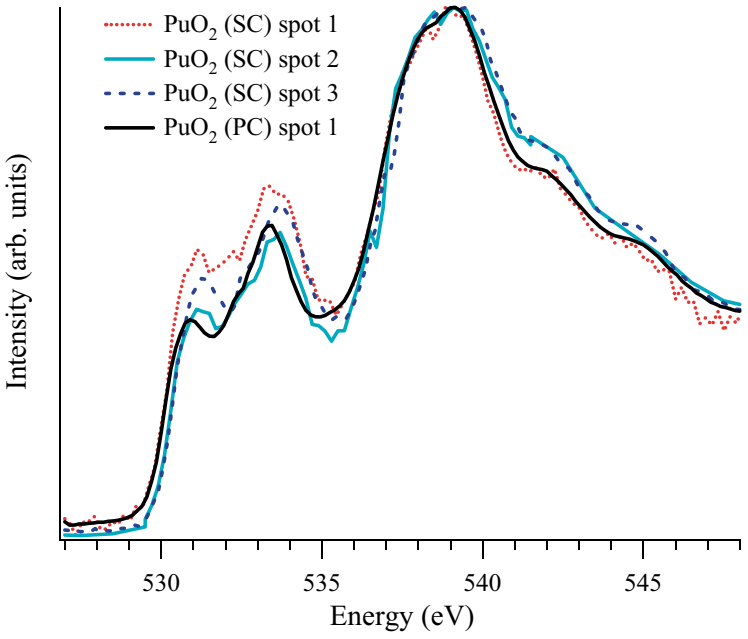

Figure 4.3: O 1*s* X-ray absorption spectra collected for three different spots on the surface of the PuO_2 single crystal (SC) together with O 1*s* XA spectrum of polycrystalline (PC) plutonium dioxide.

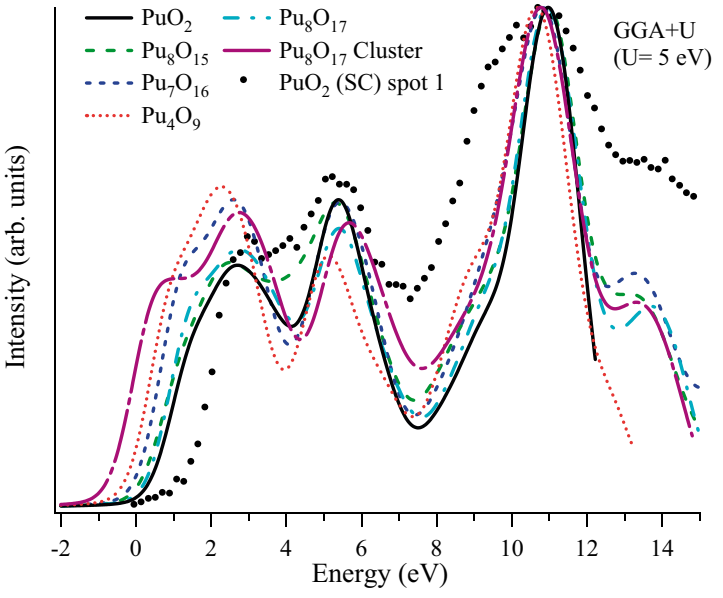

Figure 4.4: Calculated absorption spectra for the defect structures are shown together with stoichiometric PuO_2 and experimental XA spectrum.

Table 4.1: *Pu 5f and O 2p occupancy for stoichiometric plutonium dioxide, PuO_2^{1+}, PuO_2^{2+} and PuO_2 with plutonium enforced to be Pu(V).*

Compound	$Pu^{(IV)}O_2$	PuO_2^{1+}	PuO_2^{2+}	$Pu^{(V)}O_2$
Pu^{5f}	4.30	3.77	3.60	3.18
O^{2p}	4.47	4.34	4.11	4.53

Pu_4O_9 ($PuO_{2.125}$ and $PuO_{2.25}$ respectively) show growing increase of the O 2p-Pu 5f hybridization structure with increasing oxygen content yielding the largest increase for Pu_4O_9. For the measured XA spectra the behavior is opposite with higher intensity in the first peak for the single crystal PuO_2, which is believed to has Pu(IV), than for the polycrystalline sample with detected presence of the fraction of Pu with higher oxidation states.

A possible explanation for this contradicting behavior is that the redistribution of charges due to the self consistent nature of the GGA+U method causes all Pu sites in the calculation to be equal while in reality it exists inequivalent Pu sites with Pu(IV) and Pu(V) respectively.

To simulate Pu(V) sites, GGA+U calculations for PuO_2^{1+} and PuO_2^{2+} were performed using 5 eV for the Hubbard parameter U. In addition a calculation for PuO_2 with plutonium enforced to be Pu(V), where the initial density matrix was altered manually to contain only three Pu 5f valence electrons and the relaxation from this energetically unfavorable configuration was prevented by using strong Coulomb interaction (U=22 eV), was carried out. The resulting Pu 5f- and O 2p occupancy is summarized in Tab. 4.1, while the calculated total-, partial O 2p- and partial Pu 5f density of states are displayed in Fig. 4.5.

The partial O 2p DOS obtained in the Pu(V) simulations were broadened and put on the same energy scale as the measured spectra in the same way as for the LDA+U and GGA+U calculations discussed above. The resulting broadened absorption spectra for PuO_2^{1+}, PuO_2^{2+} and PuO_2 with plutonium enforced to be Pu(V) ($Pu^{(V)}O_2$) are shown in Fig. 4.5 together with that for stoichiometric PuO_2 ($Pu^{(IV)}O_2$) and one experimentally collected XA spectrum as references.

The calculated absorption spectra for PuO_2^{1+}, PuO_2^{2+} show a significant increase in intensity in the first structure, which for these compounds is split up into two features at around 1.2 and 2.6 eV respectively. The splitting of the first structure can also be seen for the Pu_8O_{17} cluster calculation, see Fig. 4.4 but is not present in the measured spectra. On the other hand, the first structure is suppressed in the GGA+U calculated XA spectrum for $Pu^{(V)}O_2$, suggesting that a linear combination of stoichiometric PuO_2 and PuO_2 with plutonium enforced to Pu(V) will yield the same behavior as for the measured XA spectra, i.e. lower intensity in the first peak for higher oxidation state.

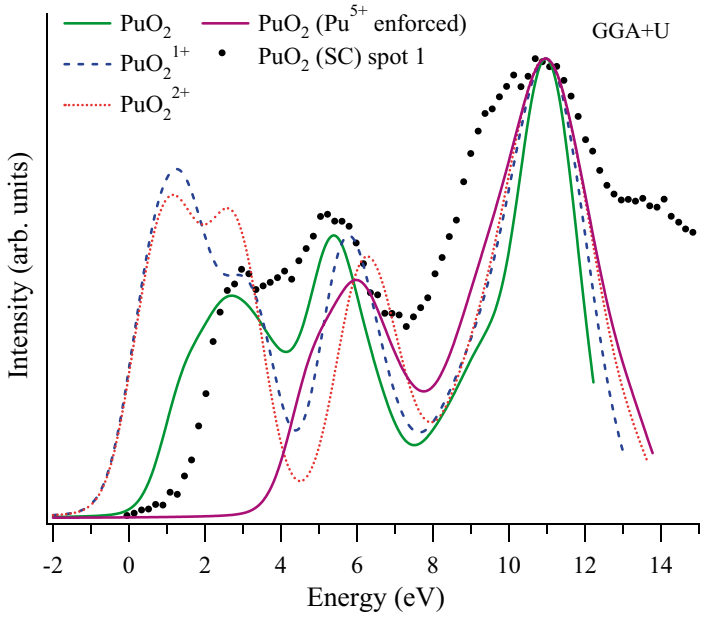

Figure 4.5: Total electron yield spectra of the polycrystalline Pu dioxide reference and Pu sorbed on Fe foil across the U 4d absorption edge.

The linear combination is constructed by adding the right proportions of $Pu^{(IV)}O_2$, and $Pu^{(V)}O_2$. Linear combinations of $Pu^{(IV)}O_2$ and $Pu^{(V)}O_2$ for; 0.25, 0.125 and 0.05 % Pu(V) are shown together with calculated stoichiometric PuO_2 and PuO_2 with plutonium enforced to Pu(V), and experimentally recorded XA spectra for single crystal and polycrystalline plutonium dioxide in Fig. 4.6.

The linearly combined spectra clearly show a trend of a decreasing intensity of the first peak with increasing fraction of Pu(V) species, which is in line with the interpretation of the experimental results. The calculated PuO_2 spectrum resembles the experimentally recorded spectrum for single crystal plutonium dioxide reasonably well, while the experimental XA spectrum for the polycrystalline sample fits in between the linearly combined $Pu^{(4.125)}O_2$ and $Pu^{(4.05)}O_2$ spectra. This indicates the presence of a $\sim$ 8% fraction Pu(V) in the polycrystalline sample, which is in line with the Pu 4*d* X-ray absorption measurements, in Fig. 4.2, and Pu 5*d* resonant inelastic X-ray scattering measurements, in Fig. 4.1, for this sample.

From Fig. 4.3 it can be seen that XA spectra collected at spot 2 and 3 on the single crystal PuO_2 show similar trend of the decreasing intensity of the first peak suggesting that those areas on the single crystal surface have some fraction of plutonium with higher oxidation state than Pu(IV).

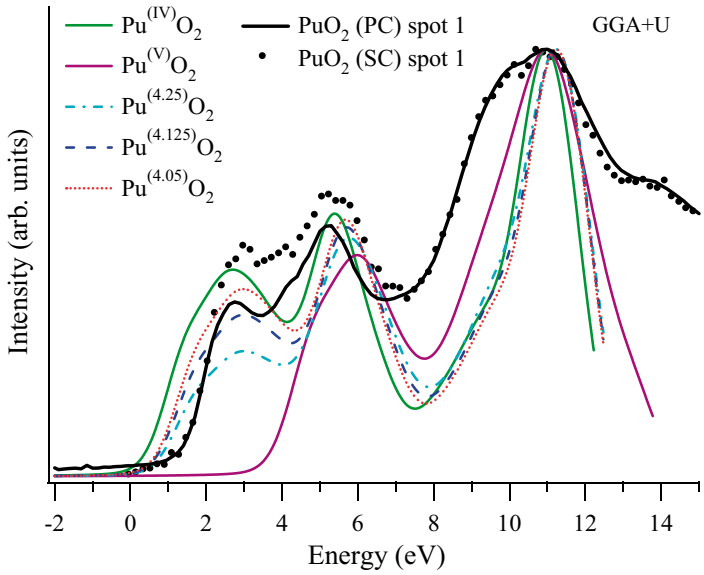

Figure 4.6: GGA+U calculated absorption spectra for stoichiometric PuO_2 and PuO_2 with plutonium enforced to Pu(V) together with linear combinations of the two calculations corresponding to $Pu^{(4.25)}O_2$, $Pu^{(4.125)}O_2$ and $Pu^{(4.05)}O_2$,and experimentally recorded XA spectra for single crystal and polycrystalline plutonium dioxide.

4.1.2 Correlation effects in light actinides

Most experimental studies of actinide materials have been conducted on the actinide side and very little data are reported for the ligands. To fully understand the correlation effects in actinide materials, also the ligands need to be studied.

Fig. 4.7 shows experimentally recorded XA and XE spectra for UO_2, NpO_2 and PuO_2. All XE spectra were recorded using similar excitation energies corresponding to the first structure in the XA spectra.

X-ray emission spectra for UO_2 and PuO_2 are similar with a weak structure around -0.3 eV and -0.7 eV respectively, the main peak at approximately -2.7 eV and a shoulder on the low energy side around -4.6 eV. The first structure is not observed in the XE spectrum for NpO_2. This results in a more asymmetrically shaped spectrum with the main peak shifted 0.2 eV towards higher energy.

The recorded O 1s X-ray absorption clearly differs between the studied compounds, especially in the low energy region where the shape and energy positions of the first three structures are distinct for each compound. For higher energies the spectra are similar with spectral features around 13.3, 16.2 19.9 and 24.6 eV. The first structure in the XA spectra arises around 2.5 eV and is clearly visible for PuO_2 while the lower spectral weight for this feature in the UO_2 and NpO_2 spectra merely causes an asymmetric shape of the more

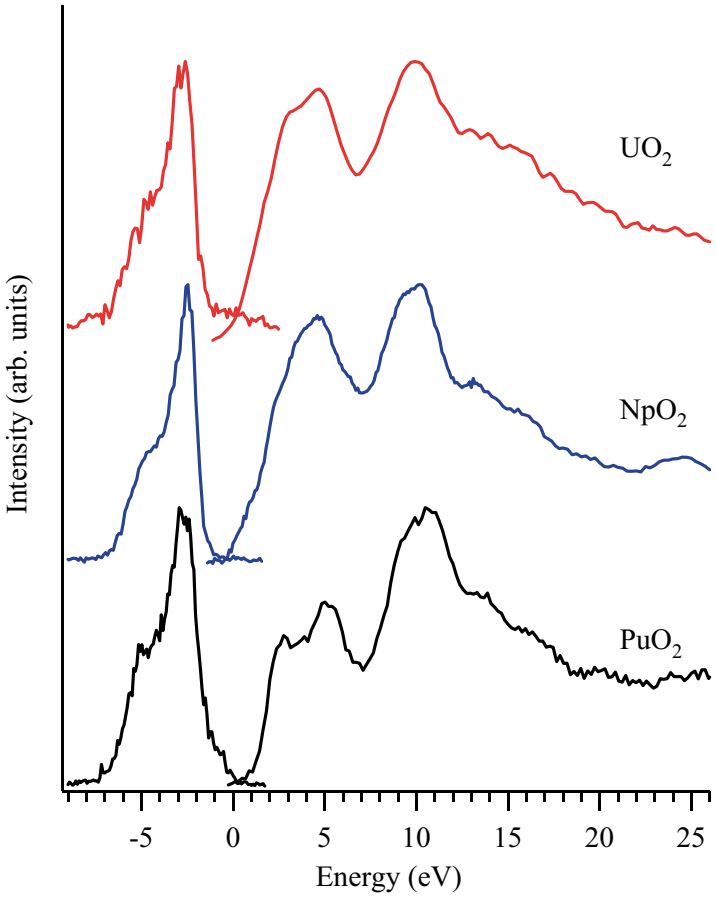

Figure 4.7: Measured O 1*s* X-ray emission and X-ray absorbtion spectra of UO_2, NpO_2 and PuO_2 on a binding energy scale.

pronounced second peak. In the UO_2 and NpO_2 XA spectra, the intensity and energy position ($\sim$4.7 eV) of the second structure are similar, while this feature arises around 5.2 eV with lower intensity for PuO_2. The energy positions of the third structure yields 9.9, 9.9 and 10.4 eV for UO_2, NpO_2 and PuO_2 respectively.

Fig. 4.8 displays LDA+U calculated total, and partial A 5f, A 6d (A=U, Np and Pu) and O p density of states for the studied actinide dioxides. From Fig. 4.7 and the discussion above it is evident that the biggest differences in the measured spectra occur in the energy region -5 - 13 eV, while at higher energies, spectra are similar for the studied samples. Hence, the discussion here will be focused on the origin of the features in XE spectra and the first three structures in the XA spectra. For brevity the notations A f and A d are used for the actinide 5f and 6d states, respectively, if not otherwise noted.

The calculated density of states (DOS) show that the low energy shoulder in the XE spectra mainly originates from O 2p states hybridizing with A d states, while the weak structure at $\sim$-0.3 eV and $\sim$-0.7 eV, respectively, in the measured UO_2 and PuO_2 spectra have predominantly O 2p-A f character. Also the main peak has mostly contribution from O 2p mixed with A f states. For NpO_2, the O 2p-Np f mixing in the 2 - 2.5 eV region will cause the main feature in the XE spectrum to shift slightly to higher values, which is in agreement with the measurements.

The energy separation between the occupied A d and A f states are similar for NpO_2 and UO_2 in the calculation while the separation is smaller for PuO_2. For the unoccupied A d and A f states, however, the behavior is different. Here, the Pu d states are well separated from the Pu f states ($\sim$1 eV) whereas there is only around 0.2 eV separation between the Np d and Np f states. In UO_2, on the other hand, the unoccupied U d and U f states are clearly overlapping.

From the bottom panel in Fig. 4.8 it is evident that the first structure in the PuO_2 XA spectrum mainly has contributions from O 2p-Pu 5f hybridization while the second peak mostly is due to O 2p states hybridizing with Pu 6d states. The small energy separation between Np d and Np f states, and the energy overlap for unoccupied U d and U f states, will result in a single structure with contributions from both O 2p-A d and O 2p-A f hybridization as these contributions cannot be resolved. For PuO_2 on the other hand, the well separated Pu d and Pu f states will give two resolved peaks in the XA spectrum with contributions from O 2p-Pu 5f and O 2p-Pu 6d hybridization respectively, which is in line with the experimental results. As there are no A f states around 10 eV for any of the dioxides, this structure in the XA spectra can be assigned to O p states hybridizing with A d states.

All LDA+U simulated XA and XE spectra were compared to the experimental spectra based on shape, energy position and energy separation between different structures as discussed above. The best fit spectra are shown in Fig. 4.9 together with measured O 2p XA and XE spectra for UO_2 (top),

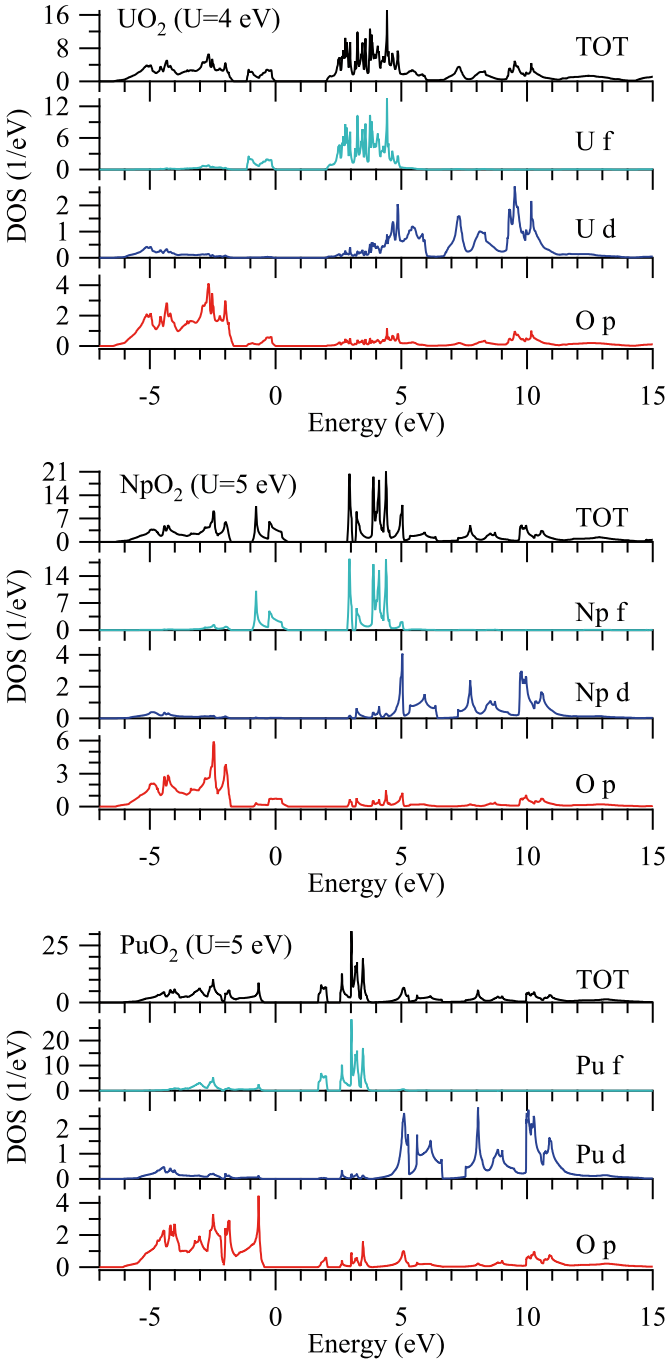

Figure 4.8: LDA+U calculated total, and partial $5f$, $6d$ density of states of actinide and O p density of states for UO_2 (top panel), NpO_2 (middle panel) and PuO_2 (bottom panel), calculated using U= 4, 5 and 5 eV respectively.

NpO_2 (middle) and PuO_2 (bottom). Here also the LDA+U calculated DOS are included and shown by dotted lines. The U-value used for each calculation is indicated in the top right corner of each panel.

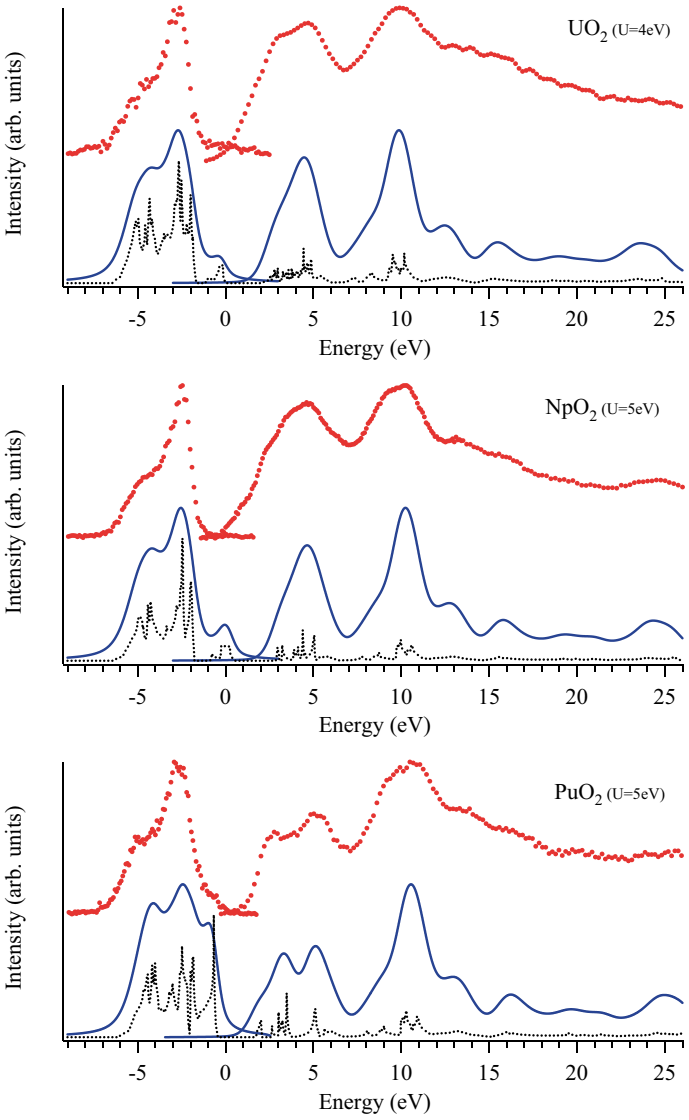

Figure 4.9: Comparison of experimentally recorded and LDA+U calculated O 2p X-ray emission and X-ray absorbtion spectra for UO_2 (top), NpO_2 (middle) and PuO_2 (bottom).

As the figure shows, the best agreement with the measured O XA and XE spectra is obtained using U=4 eV, U=5 eV and U=5 eV for UO_2, NpO_2 and PuO_2, respectively. Thus, this also suggests that the correlation effects in the experimentally recorded spectra are somewhat weaker in UO_2 in comparison

with NpO_2 and PuO_2. This is in line with the findings above and indicates that a combination of O 1s X-ray absorption and X-ray emission spectroscopies can successfully be used to study correlation effects in dioxides of light actinides.

4.2 Copper systems

Studying the electronic structure of copper compounds has been a major topic since the discovery of high temperature superconducting cuprates [25]. Extensive studies of this subject matter have since then been carried out in the hard and soft X-ray regions using different spectroscopic techniques.

In the soft X-ray regime, soft X-ray absorption spectroscopy (XAS) can be used to determine the oxidation state of copper compounds by scanning the energy over the Cu L-edge [26, 27, 28]. As chemical shifts between copper compounds with the same oxidation state are in many cases small, speciation of compounds is uncertain.

Resonant inelastic X-ray scattering (RIXS) has successfully been used in the soft X-ray region to study the local bonding environment in high-T_C superconducting cuprates and other types of complex copper systems [29, 30, 31]. In this technique, an incoming X-ray excites an electron from a core level into the valence shell and the energy of the outgoing X-ray, resulting from the recombination of the core hole with a valence electron, is measured. Since there is no core hole in the final state, the energy lost by the scattered photon is related to valence-shell excitations. The chemical selectivity and bulk sensitivity allow the study of the electronic and magnetic properties of complex materials that might be inaccessible with non resonant techniques.

It is important to study the electronic structure of simpler copper compounds for reference purposes. These references can then be used to address compounds with higher complexity, such as high-T_C superconductors or corrosion products.

4.2.1 Copper references

Fig. 4.10 shows Cu $2p$ absorption spectra for a number of copper compounds. It is obvious that the series of spectra can be divided into two classes. One in which copper is monovalent; Cu_2O and Cu_2S, and the other in which copper is divalent; CuO, $CuCl_2$, $Cu(OH)_2$, $CuSO_4$, malachite, azurite, and atacamite. For divalent compounds such as CuO, the ground state can be described as a mixture of $3d^9$ and $3d^{10}\underline{L}$ character, where $\underline{L}$ stands for a hole in the O 2p band [26, 32, 33, 34, 35]. The main peak ($2p_{3/2}$) at ~930.8 eV in the XA spectrum of CuO corresponds to the $2p^5 3d^{10}$ final state. Approximately ~20.1 eV above this peak, another structure with lower intensity appears ($2p_{1/2}$). This feature is broader than the main peak due to shorter core-hole lifetime and the

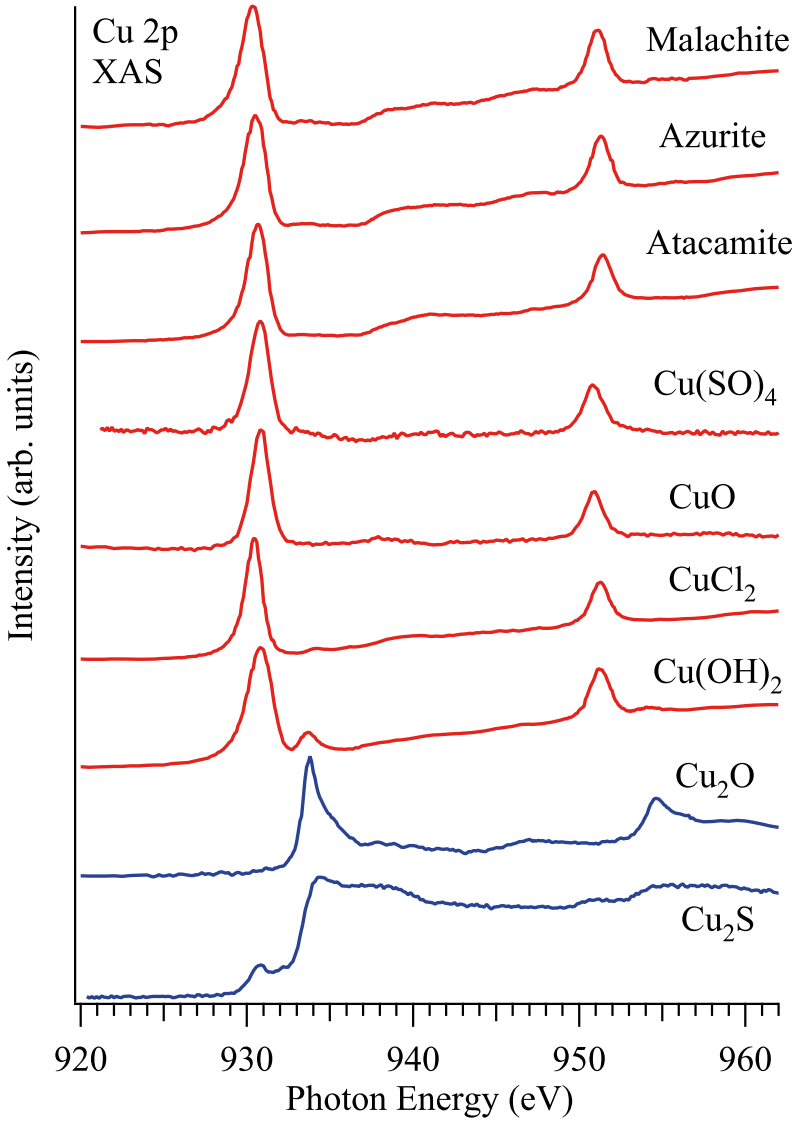

Figure 4.10: Cu 2*p* X-ray absorption (XA) spectra of CuO, Cu_2O, $CuCl_2$, Cu_2S, $Cu(OH)_2$, $CuSO_4$, malachite $Cu_2(CO_3)_2(OH)_2$, azurite $Cu_3(CO_3)_2(OH)_2$, and atacamite $CuCl_2 \cdot 3Cu(OH)_2$.

interaction with the $2p_{3/2}$ continuum. The XA spectrum of monovalent copper clearly differs from the Cu^{2+} spectra. The main line of the Cu_2O spectrum is at higher energy ($\sim$933.3 eV) due to the increased charge on the copper atoms and corresponds to excitations to the empty 4*s* level.

From Fig. 4.10 and the discussion above it is evident that Cu 2*p* X-ray absorption spectroscopy can be used for distinction of monovalent and divalent copper. However, as chemical shifts between different divalent copper species are in many cases small, see Tab. 4.2, speciation of compounds is uncertain. To overcome this shortcoming of XAS, a method utilizing RIXS for characterization of divalent copper compounds is proposed in paper VIII.

Table 4.2: *Energies of the main Cu L_3 absorption line for some divalent copper compounds, in eV.*

Compound	Cu L_3 peak (eV)
CuO	930.8
$CuSO_4$	930.8
$Cu(OH)_2$	931.0
$CuCl_2$	930.4
Atacamite ($CuCl_2 \cdot 3Cu(OH)_2$)	930.7
Azurite ($Cu_3(CO_3)_2(OH)_2$)	930.5
Malachite ($Cu_2(CO_3)_2(OH)_2$)	930.3

Fig. 4.11 shows Cu L_3 RIXS spectra for malachite $Cu_2CO_3(OH)_2$ excited at different energies indicated by dotted lines in the inserted fluorescence yield XA spectrum at the top of the panel.The malachite spectra show a number of features. The feature highest in energy, at approximately 928.5, 929.3, 930.1, 931.1, 933.1 938.8, 945.5 and 950.4 eV respectively, corresponds to elastically scattered radiation originating from the X-ray emission process in which the final state returns to the ground state again, or from reflection of the incident photons. The main structure around 1.5-2 eV below the elastic peak can be assigned to *d*-*d* excitations arising from final states with a main character of $3d^9$ configuration. The low energy tail down to $\sim$6-7 eV below the elastic peak is caused by charge transfer excitations from O 2*p* to Cu 3*d* states, and thus, reflecting continuously excited states with a main character of $3d^{10}\underline{L}$ configuration. For the spectra excited with higher energies, spectra E-H, the characteristic non resonant Cu L_α emission peak arises at $\sim$928.7 eV

Direct *d*-*d* excitations are dipole forbidden but Tanaka and Kotani [36] first showed theoretically that *d*-*d* excitations in copper are accessible with RIXS. Since then the energy of Cu *d*-*d* excitations have been thoroughly investigated, using RIXS, for cuprate superconductors and other strongly correlated systems [29, 37, 38].

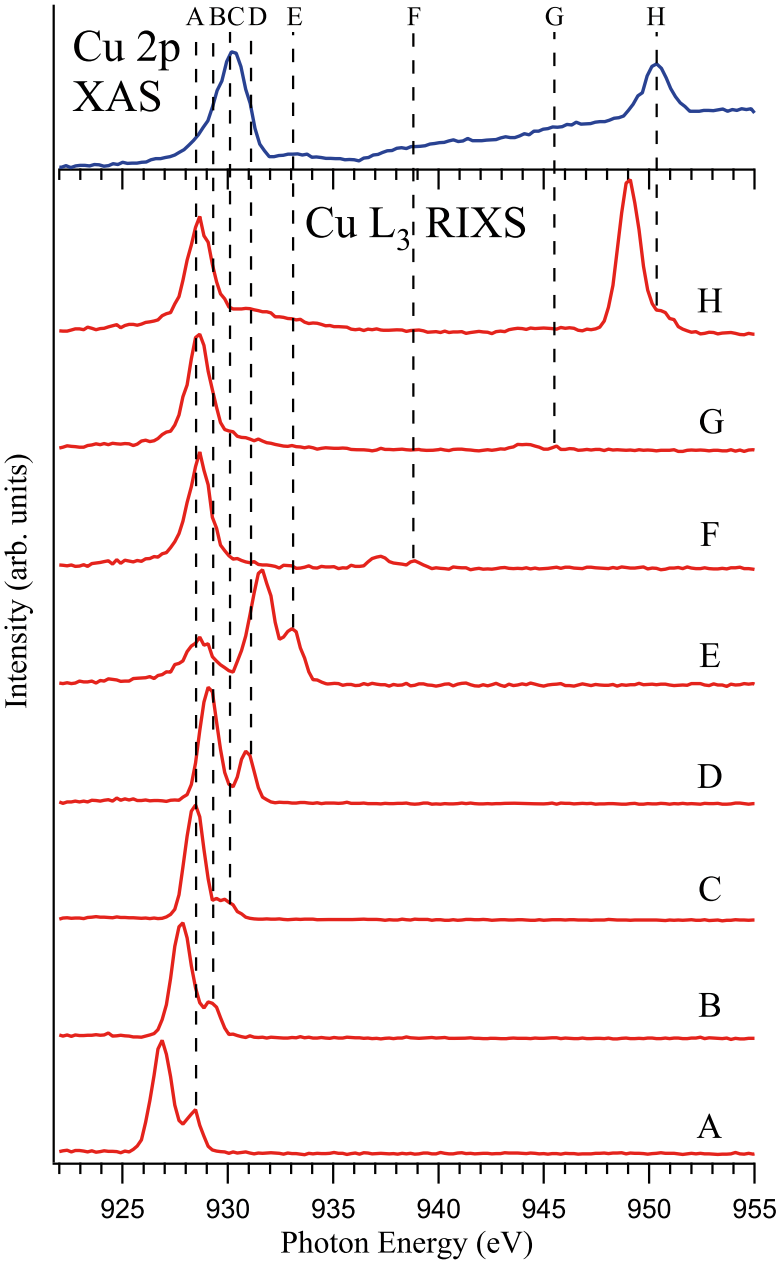

Figure 4.11: Cu L_3 RIXS spectra of malachite $Cu_2CO_3(OH)_2$, recorded at excitation energies indicated by the dotted lines in the X-ray absorption spectra shown on top.

Fig. 4.12 displays Cu L_α RIXS spectra for $CuSO_4$, $CuCl_2$, atacamite $CuCl_2{\cdot}3Cu(OH)_2$, CuO and $Cu(OH)_2$ recorded using a photon excitation of 932.9 eV. As for malachite the spectra consists of four main spectral features: elastically scattered radiation, *d-d* excitations, charge transfer excitations and normal Cu L_α emission. These features vary in intensity and energy for the studied compounds. For all compounds except $Cu(OH)_2$ the *d-d*

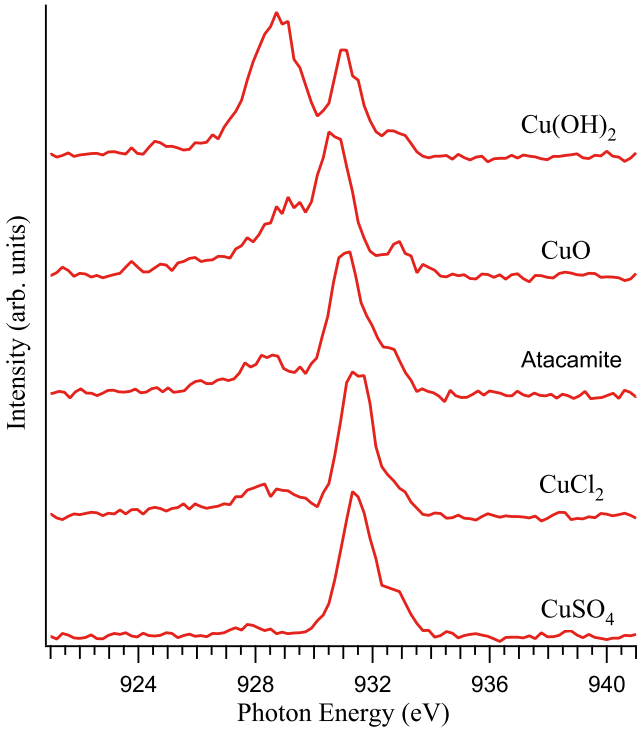

Figure 4.12: Cu L_3 RIXS spectra for different divalent copper compounds, recorded using 932.9 eV excitation energy, as indicated in the inserted $Cu(OH)_2$ XA spectrum at the top of the figure.

excitations is the most intense feature. This spectral peak arises at ∼931.5 eV for $CuSO_4$, $CuCl_2$ and atacamite, while it occurs around 931.0 eV and 930.7 eV for $Cu(OH)_2$ and CuO respectively. For $Cu(OH)_2$ and atacamite there is also a weak shoulder on the high energy side of the *d-d* excitations peak. The relative energy shift of the *d-d* excitations peak is due to difference in local symmetries around the copper site, crystal field strength and hybridization with ligand states in these compounds. This relative energy shift introduces differences in the appearance of the elastic peak. For $Cu(OH)_2$ and CuO the elastic peak is well resolved, while for the other compounds this feature appears as a shoulder on the high energy side of the *d-d* excitations peak. The

elastic peak is most intense for atacamite and $CuSO_4$, while it is weakest for $CuCl_2$ and $Cu(OH)_2$.

The charge transfer excitations are not fully resolved and for most of the samples, this feature is mixed with the characteristic L_α emission peak. For CuO though, these excitations can be seen as the low energy tail of the characteristic L_α emission peak, while for $Cu(OH)_2$, they appear as weak feature at $\sim$924.6 eV. The mixed characteristic L_α emission and charge transfer excitations feature varies widely in intensity, ranging from weak for $CuSO_4$ to strong for $Cu(OH)_2$. This line also varies in energy for the different compounds and arises around 927.8, 928.4, 928.5, 928.8 and 929.1 eV for $CuSO_4$, $CuCl_2$, atacamite, $Cu(OH)_2$ and CuO, respectively. Energy variations of the mixed characteristic L_α and charge transfer excitation feature due to changing excitation energy has previously been reported for CoO and NiO[39], but as all spectra in Fig. 4.12 are recorded using the same photon excitation, the energy variations arises from different mixing of L_α emission and charge transfer excitations between the different compounds.

From the above discussion it is evident that, by using the same excitation energy for different divalent copper compounds, RIXS provides a powerful tool for speciation of complex systems in addition to the more common use of the technique to study electronic structure. In particular, Fig. 4.12 shows that RIXS can be used *in situ* to distinguish between CuO and $Cu(OH)_2$, which is difficult with other techniques. The difference in shape, relative intensity and energy position of the elastically scattered radiation, *d-d* excitations, charge transfer excitations and characteristic Cu L_α emission introduces a number of possibilities to distinguish between different species.

In paper IX we report a similar speciation approach taken to Cu_3N, where we from resonantly excited N Kα X-ray emission spectra were able to detect fractions of copper enriched areas in copper nitride films. This was not seen in preliminary X-ray diffraction (XRD) measurements on the studied films as these measurements probe long the range order of the film structure and therefore will not see small fractions of copper enriched regions. Soft X-ray emission spectroscopy, on the other hand, is a local probe and can therefore also detect very small fractions of different copper content as long as they give rise to intensities at specific energies.

4.2.2 *In situ* corrosion studies

Copper can corrode in both gaseous and aqueous environments but since the underground repository for nuclear waste is an oxygen free environment, my research have been concentrated around aqueous corrosion.

The *in situ* aqueous corrosion measurements were conducted using the liquid cell introduced in section 3.2.2. A 10 nm copper film was deposited on the backside of 100 nm silicon nitride windows using DC-magnetron sputter-

Table 4.3: *Ion concentration, given in mmol/L (mM), in the studied synthetic groundwater[40].*

Ca^{2+}	Mg^{2+}	Na^{+}	K^{+}	Cl^{-}	HCO_3^{-}	SO_4^{2-}
0.13	0.03	2.3	0.1	1.4	1.1	0.1

ing in an ultra high vacuum chamber. The copper films were then exposed to different solutions and the interactions were monitored *in situ*.

Liquid cells with 1.5 M NaCl solution (pH=7), 1.4 mM NaCl solution with high pH (pH=11) and synthetic groundwater were studied. For the high pH solution, the pH was adjusted by adding a small amount of sodium hydroxide. The synthetic groundwater mimics a typical low ionic strength granitic groundwater from the Fenno-Scandian shield with pH=8.5[40]. Tab. 4.3 shows the ion concentration in the synthetic groundwater.

We know from Fig. 4.10 that X-ray spectroscopy can be used to determine wether copper is monovalent or divalent. As corrosion in general means a change in oxidation state, and thus a change in valency, for the studied material, XAS can be utilized to probe the oxidation of copper, see papers V and VI. However, as differences in absorption spectra between divalent copper species are in many cases small, speciation of corrosion products is uncertain. From Fig. 4.12 it is obvious that RIXS spectra provide an excellent possibility to distinguish between divalent copper systems. The possibility of using RIXS as an *in situ* tool for speciation of complex copper systems is thoroughly examined in paper VIII.

Fig. 4.13 shows a series of measurements conducted on a copper film exposed to synthetic groundwater. The XA spectrum for copper film in the fresh made cell shows contribution of both oxidized and metallic copper. The oxidized copper are mainly in the form of monovalent copper, the structure at $\sim$933.3 eV, with only a small contribution of divalent species, the peak at $\sim$930.8 eV. Metallic copper is represented by the characteristic satellite structures in the 938-942 eV range and a higher background. This is reasonable as all clean copper surfaces begin to oxidize as soon as they come into contact with air. In dry air, a very thin layer of copper oxides forms on the copper surface. This process is sometimes referred to as *toning* and it usually protects the surface from further oxidation [41]. At higher moisture levels, however, or in moist or wet environments the corrosion may progress further and not stop with toning.

After five days of exposure, the film clearly has oxidized further and the divalent and monovalent structures show similar intensities. After nine days the copper film is fully oxidized and the spectrum displays only contribution from divalent species. There are several Cu^{2+} candidates based on the shape and energy position ($\sim$930.8 eV) of the Cu^{2+} structure in the XA spectra and the film was therefore further investigated using RIXS.

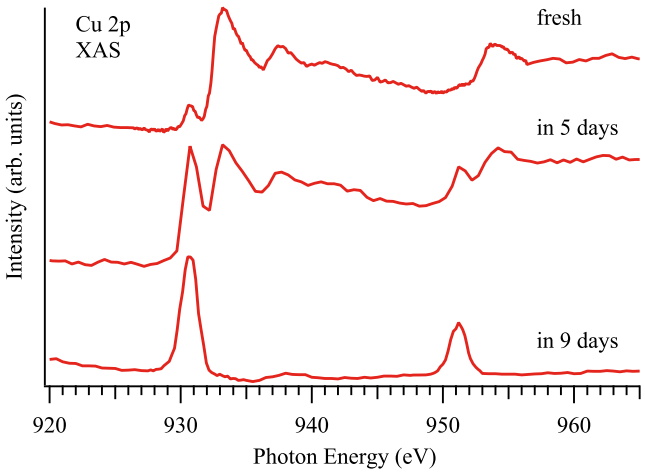

Figure 4.13: Oxidation of a copper film exposed to synthetic groundwater probed by Cu 2p X-ray absorption spectroscopy.

The *in situ* RIXS measurements were done using the 932.9 eV photon excitation on the divalent copper species as a reference. The resulting spectra from the studied liquid cells (dotted lines) are displayed in Fig. 4.14 together with suitable reference compounds (solid lines). The spectra are arranged with increasing complexity of the solutions with the most complex solution at the top of the figure.

The 1.5 M NaCl solution will have an excess of chloride ions, with which the copper film will react. From the figure it can be seen that the chemical bonding environment of the formed copper product resembles the local chemical environment of copper in copper chloride. The formation of copper chloride species is in line with calculated chemical equilibrium diagrams [42] if the pH of the solution is slightly lowered, which is reasonable due to the fast reaction and small volume of the cell, see the top panel in Fig. 4.15. It is also supported by recent X-ray diffraction results for Cu exposed to 3.5% NaCl solution reported by Guo et al. [43].

The local bonding environment of copper exposed to the 1.4 mM NaCl solution with high pH show close similarities to the local copper environment in CuO. The slightly higher energy of the *d*-*d* excitations for the oxidized copper film most likely originates from fractions of atacamite, which have similar fingerprint as CuO but with the *d*-*d* excitation peak 0.2 eV higher, see Fig. 4.12. The formation of copper oxide with fractions of atacamite is also indicated in the calculations shown in Fig. 4.15 (middle).

The spectral fingerprint of the copper film exposed to synthetic groundwater is in close agreement with the local bonding environment of copper in $Cu(OH)_2$. Thermodynamically, the stable phase should be CuO, see the bottom panel in Fig. 4.15, but the formation of $Cu(OH)_2$ is kinetically fa-

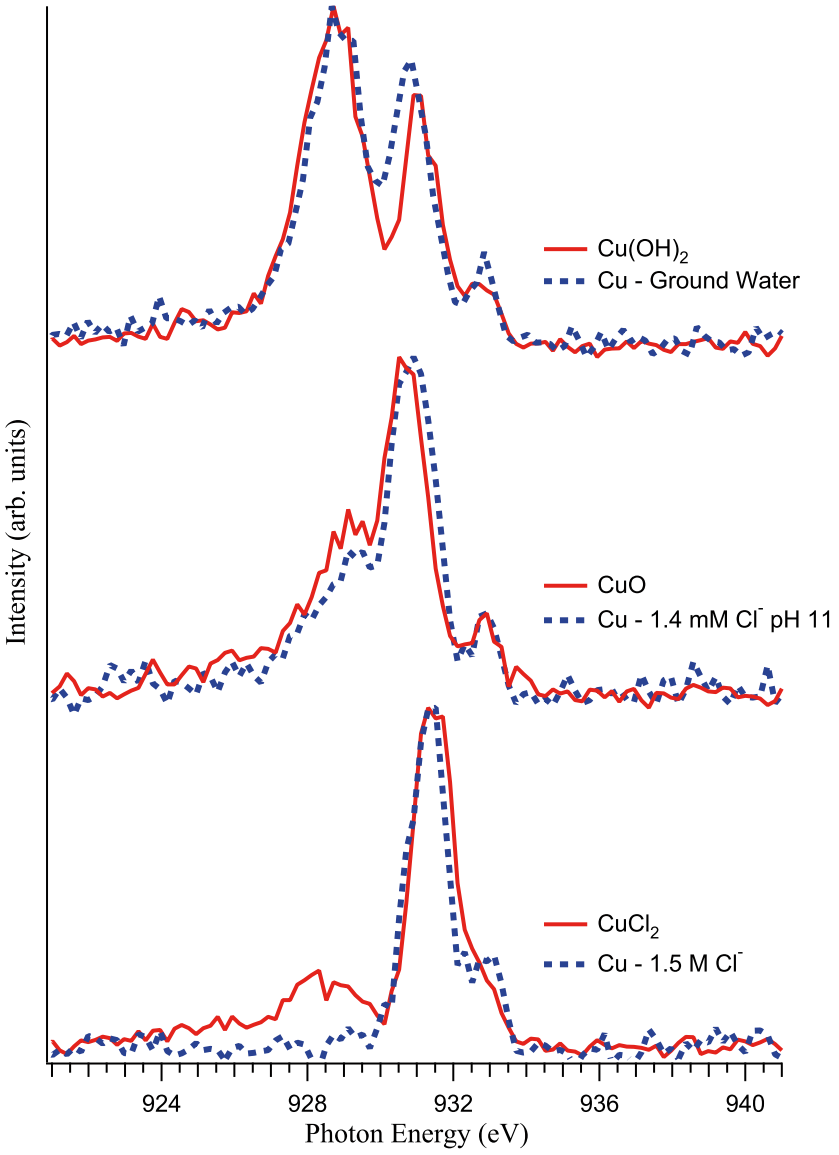

Figure 4.14: Cu L_3 RIXS spectra for copper films exposed to: 1.5 M NaCl solution, 1.4 mM NaCl solution with high pH and synthetic groundwater together with reference spectra for $CuCl_2$, CuO and $Cu(OH)_2$, recorded using 932.9 eV excitation energy.

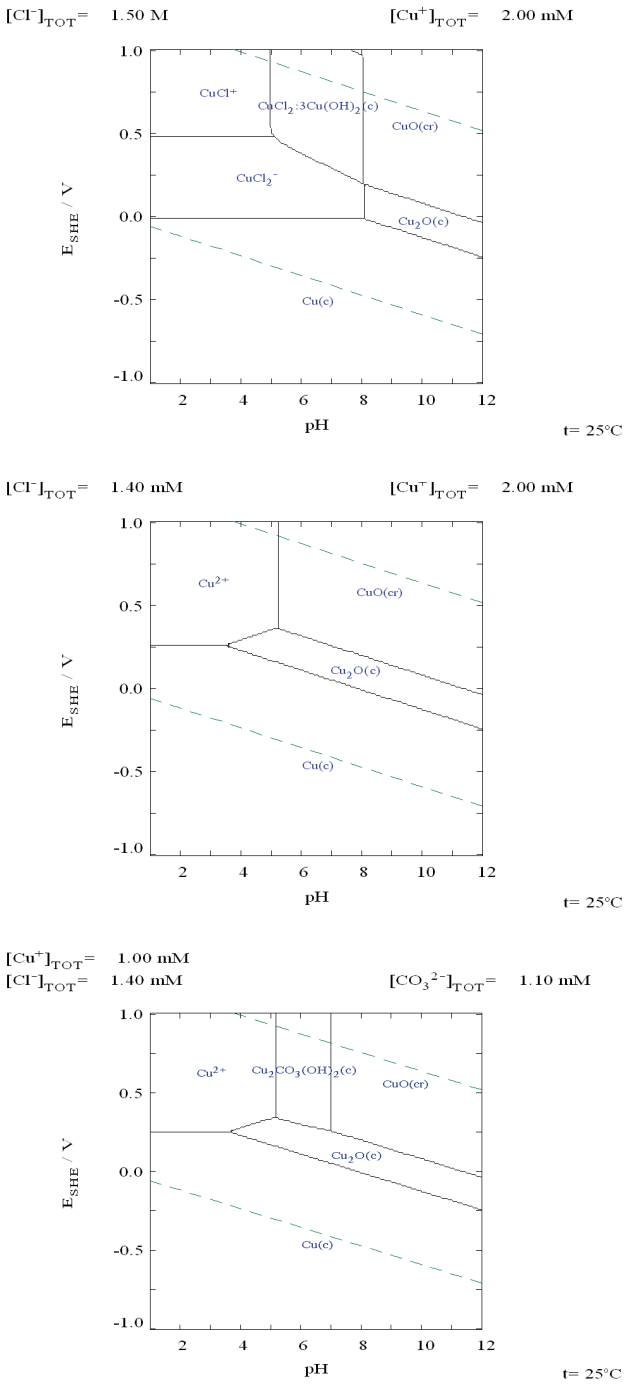

Figure 4.15: Calculated chemical equilibrium diagrams for copper exposed to 1.5 M NaCl solution (top), 1.4 mM NaCl solution with high pH (middle) and synthetic groundwater (bottom).

vored [44, 45] and the system might not have reached chemical equilibrium since the oxidation is suppressed in presence of HCO_3^- ions [28].

From Fig. 4.14 and the discussion above it is evident that, in addition to the common use of RIXS to probe the electronic structure of complex copper systems, it is also possible to use RIXS as a speciation tool by scanning the excitation energy over the Cu L edge for one compound, noting the energy where the spectral features changes the most, and use this excitation energy to study different compounds. The specific spectral fingerprints of different reference copper compounds can then be used to address more complex systems such as high-T_C superconductors or copper corrosion products.

Acknowledgments

Good research is most often a product of many competent people's work. During my PhD-studies I have had the pleasure to work with several brilliant physicists and great colleagues, who I owe many thanks for making this work possible.

First of all I would like to acknowledge my main supervisor Sergei Butorin for excellent guidance and exceptional knowledge in the field of physics and spectroscopy as well as great discussions about sports in general and Russian sports in particular. I would also like to thank my other supervisors; Joseph Nordgren for heading the USX-group and providing me the possibility to undertake this challenging and interesting project, and Lars Werme for outstanding knowledge about the processes involved in the nuclear fuel cycle as well as great assistance in proof-reading and interesting discussions.

Then I would like to recognize Leif Karlsson for guiding me through a great deal of courses and for many interesting and instructive discussions regarding atomic and molecular physics as well as for his positive attitude.

I also want to thank my present and former colleagues in the USX-group; Anders O., Anne, Barbara, Calle, Egil, Filip, Håkan, Jocke, Johan F., Johan S., Johan V., Kristina, Lage, Laurent, Marcus, Martin, Raimund and Ruben for making everyday work fun and interesting. Special thanks goes to Kristina Kvashnina for spending many long beamtime hours at ALS and MAX-lab and for all the fun during our trips.

The experimental work at ALS would not have been possible without the great assistance by Jighua Guo and the beamline staff; Aran, Tim, Per-Anders and Jau-Wern, while the measurements at MAX-lab were superbly assisted by Franz, Torsten and Tanel. Here I also would like to thank David Shuh together with Brian (ALS) and Gunnar Skarnemark (Chalmers University) for handling all radioactive materials and making these measurements possible.

I also want to acknowledge all my collaborators and co-authors not already mentioned; Anna, Mikael, Boris, Moreno, Inna and and Rolf for making samples available, and; Sergei A., Rajeev, Michi-To, Younsuk and Peter for superb first principles calculations.

During the writing of this thesis I greatly appreciated the help from Marcus, Johan F., Ruben and Leif whom together with my supervisors patiently took their time for discussions and provided valuable input. Again, I want to express my sincere gratitude to my main supervisor Sergei for his invaluable

contributions to improve my papers and this thesis. Special thanks to Johan F. and Linda Askeryd for their assistance with proofreading.

Since life isn't only about work, I'd also like to thank my friends for taking my mind off physics with numerous golf rounds and a lot of fun discussions about sports.

Finally I would like to thank my family for all their support and encouragement.

Uppsala, March 2009
Anders Modin

Summary in Swedish

Spektroskopiska studier av ljus som emitterats eller absorberats av atomer och molekyler har pågått sedan tidigt 1800-tal. Den senare tidens utveckling av de mycket ljusstarka tredje generationens synkrotronkällor, har gjort det möjligt att studera mer och mer komplexa system och idag är spektroskopi ett mycket viktigt verktyg i den moderna fysiken.

Ett sådant system är aktinider vars egenskaper till stor del påverkas av graden av lokalisering för 5f-elektronerna. Aktinider är också intressanta ur teknologisk synvinkel då de spelar en viktig roll vid slutförvar av kärnbränsle.

Den svenska metoden för slutförvar av kärnbränsle kallas för KBS-3 och bygger på tre skyddsbarriärer. Det använda kärnbränslet ska först kapslas in i koppar. De täta kopparkapslarna ska sedan placeras i urberget på cirka 500 meters djup, inbäddade i bentonitlera. När deponeringen är klar försluts tunnlar och bergrum.

För säkert slutförvar krävs således en god förståelse om aktinider i dess olika former i avfallet samt den omgivande miljöns påverkan på kopparkapseln.

I den här avhandlingen presenterar jag resultat från mjukröntgenspektroskopiska studier av de tidiga, lätta aktiniderna; uran, neptunium och plutonium samt *in situ* studier av kopparkorrosion.

Spektroskopiska studier av aktinider begränsas av en mängd lagar och regler då dessa material är radioaktiva och mycket giftiga. För att möjliggöra mätningarna utvecklades därför ett system där provet innesluts i en vakuumtät cell. För ett slutet system är regelverket kring dessa material inte lika strikta och möjligheterna till studier av aktinider ökar.

Systemet användes till studier av oxidation i kristallin plutoniumdioxid. Röntgenabsorptionspektra för syre visade att det fanns spår av plutonium med högre oxidation än Pu(IV) på vissa platser på kristallen. Detta resultat är viktigt då plutonium med högre oxidation, tex. Pu(V), har mycket högre löslighet än Pu(IV) och risken för påverkan av biosfären ökar. Dessutom indikerade en jämförelse mellan mätresultaten och resultat från *ab initio* beräkningar att PuO_2 med spår av plutonium med högre oxidation än Pu(IV) består av inekvivalenta plutoniumatomer med $Pu^{(IV)}O_2$ och $Pu^{(V)}O_2$ istället för ett system där plutoniums oxidation konstant fluktuerar mellan Pu(IV) och Pu(V).

Resultat från mätningar på syre i UO_2, NpO_2 och PuO_2 visade att en kombination av O Kα röntgenemissions- och O 1*s* röntgenabsorptionsspektroskopi kan användas till studier av elektronkorrelationseffekter i lätta aktiniddioxider.

Korrosionen av kopparkapseln i slutförvaret styrs av tillgången på korrosiva ämnen i det grundvatten som är i kontakt med kapseln. Det är därför viktig med *in situ*-studier av korrosionsprocesserna med hjälp av olika metoder.

Den elektroniska strukturen för koppar undersöktes med mjukröntgenemission och mjukröntgenabsorption. Resultaten visar att absorption kan användas till att studera valenstillståndet för koppar. Men, då skillnaderna i absorptionsspektrum är små för system med samma valenstillstånd, är identifiering svår och andra metoder behövs. Därför utvecklades en metod där resonant inelastisk röntgenspridning (Resonant inelastic X-ray scattering, RIXS) används för specificering av komplexa kopparsystem. För specifika excitationsenergier fås unika RIXS-spektra för olika kopparsystem.

Metoden tillämpades *in situ* på kopparfilmer utsatta för olika lösningar och grundvatten. Resultatet från denna studie visar att RIXS kan användas som specificeringsverktyg för komplexa processer. I synnerhet kan denna metod skilja på kopparoxid och kopparhydroxid *in situ*, vilket är svårt med andra metoder.

Bibliography

[1] Rutherford, E. *Philosophical Magazine* **21**, 669–688 (1911).

[2] Bohr, N. *Philosophical Magazine* **26**, 1–25 (1913).

[3] Bohr, N. *Philosophical Magazine* **26**, 476–502 (1913).

[4] Bohr, N. *Philosophical Magazine* **26**, 857–875 (1913).

[5] Schrödinger, E. *Annalen der Physik* **384**, 489–527 (1926).

[6] Born, M. *Z. Phys.* **37**, 863–867 (1926).

[7] Born, M. *Z. Phys.* **38**, 803–827 (1926).

[8] Atkins, P. W. and de Paula, J. *Physical Chemistry*. Oxford University Press, Great Clarendon Street, Oxford, 7 edition, (2002).

[9] Pauli, W. *Z. Phys.* **31**, 765–783 (1925).

[10] Russell, H. N. and Saunders, F. A. *Astrophys. J.* **61**, 38 (1925).

[11] Kramers, H. A. and Heisenberg, W. *Z. Phys.* **31**(1), 681–708 (1925).

[12] Kotani, A. and Shin, S. *Rev. Mod. Phys.* **73**(1), 203–246 Feb (2001).

[13] Attwood, D. *Soft X-Rays and Extreme Ultraviolet Radiation : Principles and Applications*. Cambridge University Press, (1999).

[14] Warwick, T., Heimann, P., Mossessian, D., McKinney, W., and Padmore, H. *Rev. Sci. Instrum.* **66**, 2037 (1995).

[15] Denecke, R., Vaterlein, P., Bassler, M., Wassdahl, N., Butorin, S., Nilsson, A., Rubensson, J.-E., Nordgren, J., Martensson, N., and Nyholm, R. *J. Electron Spectrosc. Relat. Phenom.* **101-103**, 971 (1999).

[16] Nordgren, J. and Nyholm, R. *Nucl. Instrum. Methods Phys. Rs. A* **246**, 242 (1986).

[17] Nordgren, J., Bray, G., Cramm, S., Nyholm, R., Rubensson, J.-E., and Wassdahl, N. *Rev. Sci. Instrum.* **60**, 1690 (1989).

[18] Henke, B. L. *X-ray interactions with matter - filter transmission* URL: `http://henke.lbl.gov/optical_constants/filter2.html`.

[19] Henke, B. L., Gullikson, E. M., and Davis, J. C. *Atomic Data and Nuclear Data Tables* **54 (2)**, 181 (1993).

[20] Holm, L.-E. and Ekström, B. The Swedish Radiation Protection Institute's Regulations SSI FS 2000:7, May (2000).

[21] Georges, A., Kotliar, G., Krauth, W., and Rozenberg, M. J. *Rev. Mod. Phys.* **68**(1), 13 Jan (1996).

[22] Anisimov, V. I., Aryasetiawan, F., and Lichtenstein, A. I. *J. Phys.: Condens. Matter* **9**(4), 767–808 (1997).

[23] Haschke, J. M., Allen, T. H., and Morales, L. A. *Science* **287**(5451), 285–287 (2000).

[24] Madic, C. *Science* **287**(5451), 243–244 (2000).

[25] Bednorz, J. G. and Müller, K. A. *Z. Phys. B.* **64**(2), 189 6 (1986).

[26] Grioni, M., Goedkoop, J. B., Schoorl, R., de Groot, F. M. F., Fuggle, J. C., Schäfers, F., Koch, E. E., Rossi, G., Esteva, J.-M., and Karnatak, R. C. *Phys. Rev. B* **39**(3), 1541–1545 Jan (1989).

[27] van der Laan, G., Westra, C., Haas, C., and Sawatzky, G. A. *Phys. Rev. B* **23**(9), 4369–4380 May (1981).

[28] Kvashnina, K. O., Butorin, S. M., Modin, A., Soroka, I., Marcellini, M., Nordgren, J., Guo, J. H., and Werme, L. *Chem. Phys. Lett.* **447**, 54 (2007).

[29] Kuiper, P., Guo, J.-H., Såthe, C., Duda, L.-C., Nordgren, J., Pothuizen, J. J. M., de Groot, F. M. F., and Sawatzky, G. A. *Phys. Rev. Lett.* **80**(23), 5204–5207 Jun (1998).

[30] Hasan, M. Z., Isaacs, E. D., Shen, Z.-X., Miller, L. L., Tsutsui, K., Tohyama, T., and Maekawa, S. *Science* **288**(5472), 1811 (2000).

[31] Kim, Y. J., Hill, J. P., Burns, C. A., Wakimoto, S., Birgeneau, R. J., Casa, D., Gog, T., and Venkataraman, C. T. *Phys. Rev. Lett.* **89**(17), 177003 Oct (2002).

[32] Grioni, M., van Acker, J. F., Czyżyk, M. T., and Fuggle, J. C. *Phys. Rev. B* **45**(7), 3309–3318 Feb (1992).

[33] van der Laan, G., Pattrick, R. A. D., Henderson, C. M. B., and Vaughan, D. J. *J. Phys. Chem. Solids* **53**(9), 1185–1190 (1992).

[34] Koster, A. S. *Molecular Physics* **26**(3), 625–632 (1973).

[35] Ghijsen, J., Tjeng, L. H., van Elp, J., Eskes, H., Westerink, J., Sawatzky, G. A., and Czyzyk, M. T. *Phys. Rev. B* **38**(16), 11322–11330 Dec (1988).

[36] Tanaka, S. and Kotani, A. *J. Phys. Soc. Jpn.* **62**, 464–467 (1993).

[37] van Veenendaal, M. *Phys. Rev. Lett.* **96**, 117404/1–4 (2006).

[38] Ghiringhelli, G., Brookes, N. B., Annese, E., Berger, H., Dallera, C., Grioni, M., Perfetti, L., Tagliaferri, A., and Braicovich, L. *Phys. Rev. Lett.* **92**(11), 117406 Mar (2004).

[39] Butorin, S. M. *J. Electron Spectrosc. Relat. Phenomena* **110**, 213 10 (2000).

[40] Vuorinen, U. and Snellman, M. Posiva working report 98-61, Posiva Oy, Helsinki, Finland, (1998).

[41] Chan, H. Y. H., Takoudis, C. G., and Weaver, M. J. *The Journal of Physical Chemistry B* **103**(2), 357–365 (1999).

[42] Puigdomenech, I. Technical report, Royal Institute of Technology, Dept. Inorg. Chemistry, Stockholm, Sweden, (1983).

[43] Guo, B., Zhang, P., Jin, Y., and Cheng, S. *Rare Metals* **27**(3), 324 – 328 (2008).

[44] Shoesmith, D. W., Rummery, T. E., Owen, D., and Lee, W. *J. Electrochem. Soc.* **123**(6), 790–799 (1976).

[45] Burke, L. D., Ahern, M. J. G., and Ryan, T. G. *J. Electrochem. Soc.* **137**(2), 553–561 (1990).

Acta Universitatis Upsaliensis

Digital Comprehensive Summaries of Uppsala Dissertations from the Faculty of Science and Technology 626

Editor: The Dean of the Faculty of Science and Technology

A doctoral dissertation from the Faculty of Science and Technology, Uppsala University, is usually a summary of a number of papers. A few copies of the complete dissertation are kept at major Swedish research libraries, while the summary alone is distributed internationally through the series Digital Comprehensive Summaries of Uppsala Dissertations from the Faculty of Science and Technology. (Prior to January, 2005, the series was published under the title "Comprehensive Summaries of Uppsala Dissertations from the Faculty of Science and Technology".)

Distribution: publications.uu.se
urn:nbn:se:uu:diva-100221

ACTA
UNIVERSITATIS
UPSALIENSIS
UPPSALA
2009